UNIVERSITY OF CALIFORNIA
RIVERSIDE

Titanium MEMS Technology Development for Drug Delivery and Microfluidic Applications

A Dissertation submitted in partial satisfaction
of the requirements for the degree of

Doctor of Philosophy

in

Mechanical Engineering

by

Omid Khandan

June 2015

Dissertation Committee:
Dr. Masaru P. Rao, Chairperson
Dr. Guillermo Aguilar
Dr. Hideaki Tsutsui

The Dissertation of Omid Khandan is approved:

_____

_____

_____

Committee Chairperson

University of California, Riverside

ACKNOWLEDGEMENTS

First and foremost, I would like to acknowledge my advisor, Dr. Masa Rao, whom I cannot thank enough for his continual support, mentorship, and teaching throughout my graduate career. Thank you for motivating and encouraging me to persist at times when experiments failed and all hope seemed lost. Your guidance during those pressing times not only helped me to develop solutions, but also helped me grow as a researcher and as a person.

I would like to thank all the labmates I had the great opportunity to work alongside in the Biomedical Microdevices Laboratory. Thank you all for your friendship and support throughout the research experience. I would like to especially thank Shannon Gott, Clara Zhang, Ryan Peck, and Harish Dixit for making my time at UCR more enjoyable and productive. Shannon, it was a pleasure developing titanium etching with you, and I thank you for joining me on those long drives to and late nights working in the UCSB cleanroom; it was challenging, but your help and continued support helped me get through it. To Clara, Ryan, and Harish, I am grateful for the friendships we developed, both inside and outside of the lab, and for always providing insightful discussions on the development of our research.

I would like to thank Dr. Malik Kahook for his willingness to collaborate on the microneedle work, and Amin Famili for his assistance with preliminary microneedle penetration studies. Thank you to Chris Salinas and Steven Herrera for their assistance with the mechanical testing of the microneedles, and to Daniel Stark for assisting with preliminary titanium anodic bonding development. Thank you to Dr. Victor Rodgers for

graciously allowing our research group access to his laboratory's high-pressure syringe pump and spectrophotometer, and to Dr. Hidaeki Tsutsui for providing access to his laboratory's fluorescent microscope. These professors' assistance was crucial in the development of my work. I would also like to thank Dr. David Carter for his assistance with tissue histological sectioning; and most importantly, I would like to thank Bob Wright. Bob not only assisted with the fabrication of various testing fixtures, but also provided a great mentorship and friendship. Bob, your expertise and guidance helped me grow as an engineer, and our conversations always inspired me to be a better person and produce better work.

I would also like to acknowledge the University of California Riverside Regents' Faculty Fellowship for partial support of this work.

To the undergraduate researchers who contributed in various ways to a number of projects throughout the years – Each of you helped me grow as leader and as a teacher, and I thank you for those lessons. Fady Hanna, Sahithi Rani, Amirr Neal, Rachel Ye, Pierre Genot, and Alexander Chang, I am certain all of you will excel in your future academic and professional careers; I wish you all the best.

Finally, I would like to thank my family and friends for their continued love and care through my graduate school career. Thank you to my mom, dad, sister, and aunt for having such a supportive presence in my life, and for always encouraging—as well as challenging—me to do and be my best. Most importantly, I would like to thank Julisa for her love and support over the past two years. You have helped me grow to become a

better writer, researcher, leader, father, and individual. I am forever grateful to have you in my life.

Finally, I would like to acknowledge my feathered and furry ones, Luke, Penny, and Perry for being in my life. They provide me with the necessary distractions to keep my sanity during the most stressful times. Their unconditional love as well as their fascination to understand and experience all things has changed my view of the world forever.

DEDICATION

To all my creatures. I love you all forever.

ABSTRACT OF THE DISSERTATION

Titanium MEMS Technology Development for Drug Delivery and Microfluidic Applications

by

Omid Khandan

Doctor of Philosophy, Graduate Program in Mechanical Engineering
University of California, Riverside, June 2015
Dr. Masaru P. Rao, Chairperson

The use of microelectromechanical systems (MEMS) technology in medical and biological applications has increased dramatically in the past decade due to the potential for enhanced sensitivity, functionality, and performance associated with the miniaturization of devices, as well as the market potential for low-cost, personalized medicine. However, the utility of such devices in clinical medicine is ultimately limited due to factors associated with prevailing micromachined materials such as silicon, as it poses concerns of safety and reliability due to its intrinsically brittle properties, making it prone to catastrophic failure. Recent advances in titanium (Ti) micromachining provides an opportunity to create devices with enhanced safety and performance due to its proven biocompatibility and high fracture toughness, which causes it to fail by means of graceful, plasticity-based deformation. Motivated by this opportunity, we discuss our efforts to advance Ti MEMS technology in two ways: 1) Through the development of titanium-based microneedles (MNs) that seek to provide a safer, simpler, and more efficacious means of ocular drug delivery, and 2) Through the advancement of Ti anodic

bonding for future realization of robust microfluidic devices for photocatalysis applications.

As for the first of these thrusts, we show that MN devices with in-plane geometry and through-thickness fenestrations that serve as drug reservoirs for passive delivery via diffusive transport from fast-dissolving coatings can be fabricated utilizing Ti deep reactive ion etching (Ti DRIE). Our mechanical testing and finite element analysis (FEA) results suggest that these devices possess sufficient stiffness for reliable corneal insertion. Our MN coating studies show that, relative to solid MNs of identical shank dimension, fenestrated devices can increase drug carrying capacity by 5-fold. Furthermore, we demonstrate that through-etched fenestrations provide a protective cavity for delivering drugs subsurface, thereby enhancing delivery efficiencies in an ex vivo rabbit cornea model. Collectively, these results show the potential embodied in developing Ti MNs for effective, minimally invasive, and low-cost ocular drug delivery.

Additionally, or the second of these thrusts, we report the development of an anodic bonding process that allows, for the first time, high-strength joining of bulk Ti and glass substrates at the wafer-scale, without need for interlayers or adhesives. We demonstrate that uniform, full-wafer bonding can be achieved at temperatures as low as 250°C, and that failure during burst pressure testing occurs via crack propagation through the glass, rather than the Ti/glass interface, thus demonstrating the robustness of the bonding. Moreover, using optimized bonding conditions, we demonstrate the fabrication of rudimentary Ti/glass-based microfluidic devices at the wafer-scale, and their leak-free operation under pressure-driven flow. Finally, we demonstrate the monolithic integration

of nanoporous titanium dioxide within such devices, thus illustrating the promise embodied in Ti anodic bonding for future realization of robust microfluidic devices for photocatalysis applications. Together, these results demonstrate the potential embodied in utilizing Ti MEMS technology for the fabrication of novel drug delivery and microfluidic systems with enhanced robustness, safety, and performance.

TABLE OF CONTENTS

LIST OF FIGURES

LIST OF TABLES

1 INTRODUCTION

1.1. Materials and Methods for MEMS

It is well known that single crystal silicon (Si) is the most widely used material in the integrated circuit (IC) industry, primarily due to its ease of machinability, advantageous semiconducting properties, and relatively low cost, all of which make it ideal for use in microelectronics. As a result, the development of microelectromechanical systems (MEMS) technology has relied heavily on the development of Si-based devices. Many techniques are utilized to fabricate MEMS devices, but in general, MEMS fabrication can be categorized as surface micromachining, bulk micromachining, and micromolding (Madou 2002).

Surface micromachining utilizes thin film deposition and sputtering techniques to deposit and selectively remove various materials on a substrate or wafer. This process utilizes a combination of structural and sacrificial layering with lithographic patterning and etching techniques to create complex three-dimensional structures and features. Typical thin film materials used for surface micromachining include polysilicon, silicon dioxide, silicon nitride, metals (gold, titanium, nickel, aluminium) and metal oxides, and polymers (Bustillo, Howe, and Muller 1998). Although the combination of structural and sacrificial layering allows for many possibilities for fabrication, structures are ultimately limited in height and aspect-ratio due to residual film strain that results from prevailing deposition techniques.

Bulk micromachining uses selective etching and patterning techniques to remove material from a substrate, thereby enabling the fabrication of features with micro- and nano-scale features. Unlike surface micromachining, bulk micromachining allows for the

fabrication of high-aspect-ratio structures inside the substrate, i.e., devices are fabricated from within the initial substrate. Photolithographic techniques are used to define mask patterns on a substrate, followed by dry and wet etching to form structures and features. Typical dry etching methods utilize high density plasma to chemically and mechanically etch materials. Forms of plasma etching include isotropic reactive ion etching (RIE) and anisotropic deep reactive ion etching (DRIE). Wet etchants such as potassium hydroxide (KOH) or tetramethylammonium hydroxide (TMAH) are also used to selectively etch materials or particular crystollographic orientations within Si substrates. Similarly, hydrofluoric acid (HF) is often used to selectively wet etch silicon dioxide (SiO_2) or particular deposited metals from a Si substrate. Gas or vapor phase etching is also common, and typically uses xenon difluoride (XeF_2) gas or HF vapor (Madou 2002). Bulk micromachining is commonly combined with surface micromachining techniques to develop highly complex three-dimension MEMS with multifunctionality.

Micromolding utilizes pattern transfering and stamping techniques to fabricate MEMS structures and devices at the micrometer and nanometer scale. Typical micromolded materials consist of elastomeric polymers such as polydimethysiloxane (PDMS). The technique of micromolding is generally considered cheaper than surface or bulk micromachining due to lower processing complexity and reduced material costs. Micromolding is often used in combination with the aformentioned micromachining techniques to fabricate complex master molds for pattern transfer. For example, micromolding can be combined with surface micromachining techniques such as nickel electroplating to deposit thick metal films on SU-8 molds, thereby enabling high-aspect-

ratio MEMS structures. While polymer devices suffer from low moduli and stiffness, the ability to fabricate devices quickly and affordably has made micromolding a well-suited technique for many applications (Saliterman 2006).

1.2. Biomedical Microdevices

The demand from the IC industry for smaller and more affordable MEMS with greater sensitivity and performance has resulted in continued advancement in infastructure and tooling used to fabricate such devices. As a result, new markets for MEMS technology have emerged, and include biomedical microelectromechanical systems (bioMEMS), also referred to as biomedical microdevices, lab-on-a-chip (LOC) systems, and micro total analysis systems (μTAS). These technologies utilize existing and emerging semiconductor fabrication techniques to fabricate devices that utilize mechanical, electrical, and fluidic systems at the micro-scale for biological applications, diagnostics, and point-of-care treatment. Illustrative examples of such devices include microneedles for drug delivery, implantable microelectrodes for neural stimulation, miniturized biosensors for glucose monitoring, organ-on-a-chip systems for human physiological studies, microfluidic systems for single cell and DNA analysis, and microreactors for hydrogen generation (Saliterman 2006). The miniturization of medical devices provides advantages over their macro-scale counterparts, namely due to the increase in sensitivity and detection capabilities at the micro- and nano-scale, enhanced mechanical and fluidic performance using microprecision, and improved capabilities using multifunctional materials. Furthermore, semiconductor processing allows

manufacturing for scalability, which helps lower costs, thus making such devices attractive from a commercialization standpoint.

However, the ultimate utility of such devices will be dictated by their ability to be used safely and reliably, particularly when intended for clinical applications such as drug delivery or for implantation in the body. As such, some micromachining materials have limited applications due to their intrinsic material properties. For example, Si and glass are intrinsically brittle and make them prone to catastrophic failure, while polymers suffer from low moduli and hardness, limiting their potential for high strength applications; meanwhile, deposited thin films are largely limited to a few microns at best, severely limiting their utility and performance. In this relatively new field of bioMEMS, the development of safe, reliable, and low-cost devices is critically important for ensuring potential for clinical translation. Recent developments of titanium-based devices have shown potential to meet some these demands unable to be met by traditional semiconductor industry materials.

1.3. Bulk Titanium Micromachining

The first developments for bulk micromachining Ti were published in 2004 by M. F. Aimi et al., and utilized a cyclic etch process to enable, for the first time, high-aspect-ratio micromachining of bulk Ti substrates. The metal anisotropic reactive ion etching with oxidation (MARIO) process used cyclic plasma etch and passivation steps to enable anisotropic deep etching of bulk Ti. The process used a Cl_2/Ar plasma to etch material in the vertical direction, and a O_2 plasma to passivate the floors and sidewalls of structures.

Due to the anisotropy of the plasma, subsequent etch steps would continue to etch vertically, while generated sidewall passivation would inhibit lateral etching of features. As shown in Figure 1-1, this cyclic plasma etch process enabled the fabrication of high-aspect-ratio (HAR) Ti structures. This process is in stark contrast from existing Ti surface micromachining thin film sputtering techniques, which are ultimately constrained in height due to residual film stresses that result from deposition. Although compatible wet etching techniques exist for Ti, they are isotropic, and ultimately limit the features that can be produced, particularly at the microscale. The MARIO process enabled HAR micromachining of 500 μm Ti sheets (i.e., wafers) down to 10 μm thickness Ti foils, thereby creating the opportunity to fabricate novel Ti MEMS devices with enhanced material properties beyond those used in traditional semiconductor-based MEMS.

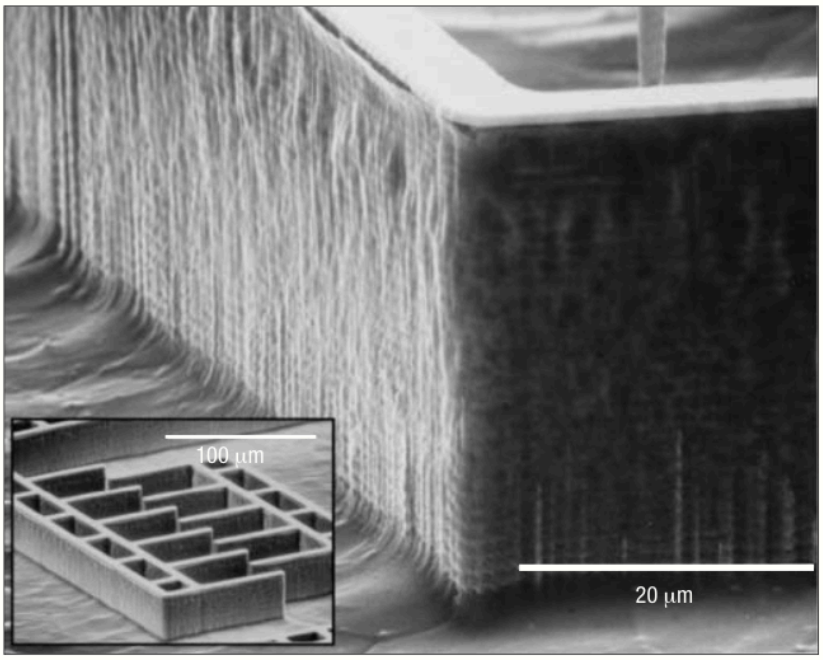

Figure 1-1. Scanning electron micrograph of bulk micromachined Ti comb drive actuator fabricated using the MARIO process (Marco F. Aimi et al. 2004).

Soon after the development of the MARIO process, an improved technique for Ti DRIE emerged. By omitting the O_2 passivation step from the MARIO process, the Titanium Inductively Coupled Deep Reactive Ion Etching (TIDE) process utilized a noncyclic Cl_2/Ar etch chemistry to fabricate HAR Ti structures with smooth sidewalls due to the elimination of sidewall scalloping. Etch rates in excess of 2 μm/min were achieved. The anisotropic nature of the Ti deep reactive ion etch (Ti DRIE) process was believed to be a result of sidewall passivation produced by condensation of etch by products on the feature sidewalls during the etch, which resulted in sidewall passivation during the etch. Figure 1-2 shows one of the first demonstrated devices fabricated using the improved Ti DRIE process.

These recent advancements in Ti micromachining provides one solution to the shortcomings of the previously discussed micromachined materials, primarily due to the enhanced biocompatibility and high fracture toughness of Ti. Ti provides opportunity for enhanced device safety due to its ductility, which causes it to deform by means of graceful, plasticity-based failure when subjected to external loading. These factors can increase safety and reliability relative to conventional materials fabricated from Si or glass, which are prone to catastrophic failure due to their intrinsic brittle properties. Ti is also a proven biocompatible metal with a long history of use in dental and orthopedic implants, thus proving its increased physiological compatibility for novel biomedical microdevices.

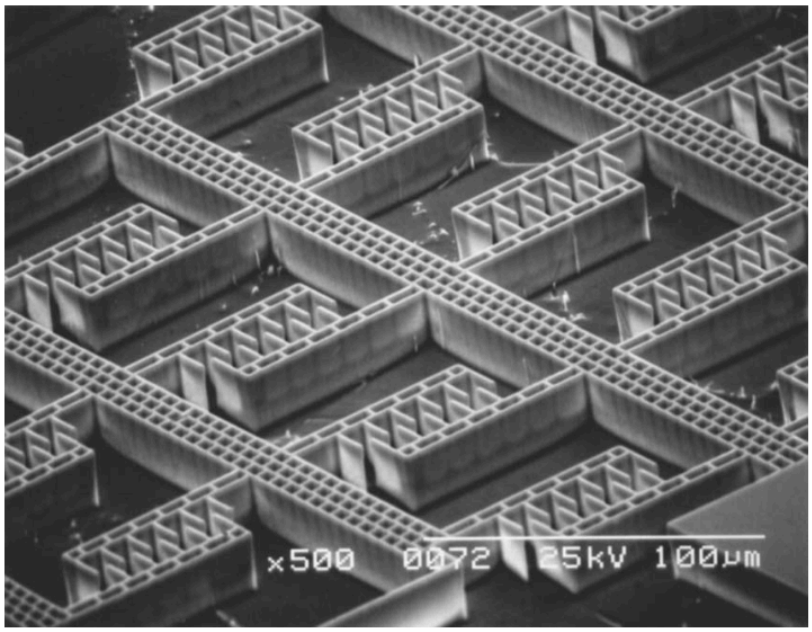

Figure 1-2. Scanning electron micrograph of bulk micromachined Ti comb drive actuator fabricated using the TIDE process (Emily R. Parker et al. 2005).

1.4. Titanium MEMS, BioMEMS and Microfluidic Devices

Since development of the Ti DRIE processes, new opportunities exist for exploiting the advantageous properties of Ti for realization of novel MEMS, BioMEMS, and microfluidic devices with enhanced robustness, performance, and functionality. Examples of such devices include microneedles for transdermal drug delivery (ER Parker et al. 2007), thin-foil devices for biomolecule separation and characterization (Zhang et al. 2008), large-area thermal ground planes for electronics cooling (Ding et al. 2010; Abu Samah Zuruzi et al. 2013), and rationally nanopatterned substrates for improved cellular response (Vandrangi et al. 2014). Furthermore, Ti DRIE provides the potential for

scalability due to ease of integration with existing semiconductor processing facilities. However, to date, studies of such Ti-based devices have been limited compared to studies of devices based on conventional micromachined materials, such as Si. The lack of existing application specific technologies, coupled with the opportunity to create devices with enhanced safety, reliability, and performance, motivates our research to further develop such technologies.

1.5. Dissertation Outline

The work outlined in this dissertation seeks to further develop Ti MEMS technology through development of 1) fenestrated Ti microneedles for ocular drug delivery, and 2) a Ti anodic bonding process for microfluidic applications. Chapter 2 of this dissertation will discuss Ti micromachining and the methods for fabricating such devices. Chapter 3 will cover the development of novel fenestrated Ti microneedles which seek to provide a safer and more efficient means for treating posterior ocular diseases. Chapter 4 will discuss the development of a new Ti anodic bonding process that enables, for the first time, bonding of optically transparent substrates to Ti, at the wafer scale. Finally, Chapter 5 will conclude the dissertation and provide some ideas for future studies.

2 DEEP REACTIVE ION ETCHING OF BULK TITANIUM

2.1. Introduction

To better understand the development of Ti MEMS technology, it is important discuss the methods and techniques used to fabricate such devices. This chapter will provide a brief background and understanding of the materials and micromanufacturing technologies that are used to the develop Ti MEMS.

2.2. Materials

Ti DRIE processes rely on the use of high purity material to ensure chemical compatability for fabricating features at the microscale. For this work, Grade 1 Commercially Pure (CP) Ti was used. Ti materials are fabricated from stock ingots using standard metalworking cold rolling processes. This technique allows for sheets to be manufactured from 500 μm down to 10 μm thickness. Current limitations to manufacturing practices limit sheets under 100 μm thickness to a crudely polished finish, while sheets of thickness 100 μm or greater can be polished to a mirror finish. To provide improved compatability with existing semiconductor processes and tooling, 500 μm thickness Ti sheets are shaped to standard 100 μm diameter wafers size by blanking with a press machine. For the work outlined in this dissertation, Grade 1 CP Ti in the form of 50 μm thickness sheets (Fine Metals Co., Ashland, VA) and 100 mm diameter, 500 μm thickness single sided polished wafers (Tokyo Stainless Grinding Co., Ltd, Tokyo, Japan) were used.

2.3. Deposition

As previously discussed, a number of physical or chemical deposition techniques exist to form thin layers of solid material on substrate surfaces. One such technique uses physical vapor deposition (PVD) uses sputtering or evaporative processes to physically deposit material on a substrate surface. Chemical vapor deposition (CVD) is the process that used gases or vapors at high processing temperatures (typically > 500°C) which react to grow films on a substrate surface. This process is widely used in semiconductor fabrication for its ability to grow uniform, high quality films on substrates. However, for certain device specific processes, lower operating temperatures are required. Plasma enhanced chemical vapor deposition (PECVD) uses a parrallel plate electrode setup under vacuum to energize reactive gas species which then deposit on the substrate surface. Plasma enhanced depostion is advantageous over other processes such as CVD due to lower processing temperatures and shorter times required to achieve the same film thicknesses. Typical thin films produced using PECVD include SiO_2, SiN, and X (Madou 2002). Inductively coupled plasma (ICP) PECVD uses electromagnetic induction to generate high-density plasma. ICP PECVD is capable of depositing higher density thin films which provide increased resistance to plasma etching relative to those produced using standard PECVD systems. Higher density films provide increased etch selectivity between the sacrificial mask and substrate to be etched, thereby improving processing capabilities for deep etching HAR structures and through-etching substrates.

For the work outlined in this dissertation, ICP PECVD was used to deposit thin SiO_2 masks on Ti substrates, which provided good selectivity and chemical stability for our Ti DRIE process.

2.4. Lithography

Lithography refers to the process of image transfer and printing, and is used in semiconductor processing to project mask patterns onto the thin films or bulk substrates for subsequent microfabrication. The most common technique used in semiconductor processing is photolithography, which uses light and a photomask to transfer patterns into a light-sensitive polymer called photoresist (PR). Depending on the type of PR used (e.g., positive or negative PR), exposed regions of the film undergo certain chemical reactions that cause strengthening or weakening of their polymer chain bonds. Subsequent development using alkaline solutions cause weakly bonded areas to be removed, leaving behind PR for the desired mask pattern. For the work outlined in this dissertation, hard contact lithography was used for its ability to provide sufficient resolution of features with critical dimension greater than ~5 μm.

2.5. Titanium Deep Reactive Ion Etching

Titanium inductively coupled plasma deep reactive ion etching a.k.a., Ti DRIE, uses plasma etching to selectively etch patterned Ti substrates at the micron- and sub-micron level. As previously discussed, Ti DRIE uses a Cl_2/Ar plasma to etch Ti substrates by mechanical and chemical means. High density plasma formed in the

reactive chamber generates ions and free radicals which are then bombarded to the surface of the substrate. The physical bombardment causes exposed material to be etched from the surface. The resulting etch products released from the bulk of the substrate cause chemical reactions with the reactive species in the plasma. These unique reactive materials passivate the sidewalls of etched structures, thereby enabling the anisotropic etch characteristics of Ti DRIE. Adding O_2 to the etch process leads to more passivation during the etch, which may be necessary to improve the sidewall profile but may also cause micromasking.

2.6. Passivation and Oxide Removal

Residual oxide removal is necessary after Ti DRIE to ensure fabricated devices remain completely from Ti. Through the development of devices discussed in this dissertation, various techniques to remove remaining mask oxide were explored. Primarily, these methods utilized dry etching techniques to selectively remove remaining mask oxide. Based on previous studies of etching deposited SiO_2 thin films, RIE using combinations of CF_4/O_2 and SF_6/Ar plasma chemistry were tested. As will be discussed later in this dissertation, it was found that using

Furthermore, a technique to remove resulting sidewall passivation layers was necessary for fabrication of devices with smooth sidewalls. A number of dry etch processes were explored with no success. Plasma etching based on CF_4 or CHF_3 consistantly resulted in redeposition and micromasking on the Ti surface. It was determined that devices fabricated using Ti DRIE were not suited for fluorine-based etch

chemistries. Instead, a brief 1 min wet etch using TFTN (Transcene Company, Inc., Danvers, MA) was enough to aid in the release of the passivation layer after Ti DRIE. Subsequent devices were remounted to a Si carrier using photoresist and etched using a SF_6/Ar plasma to remove remaining mask oxide. This resulted in Ti MEMS with no remaining sidewall passivation films nor remaining mask oxide. More details of device fabrication processes are given in Appendix A-E.

3 TITANIUM MICRONEEDLES FOR OCULAR DRUG DELIVERY

3.1. Introduction

3.1.1. Ocular Diseases

The motivation for this research comes from the growing need to effectively treat posterior segment ocular diseases, such as age-related macular degeneration (AMD). AMD is an age-related chronic eye disease caused by deterioration in the macula region of the eye, which is responsible for central vision. AMD disease currently affects more than 1.75 million individuals in the United States, and is expected to more than double by 2020 (The Eye Diseases Prevalence Research Group 2004). It is the number one cause of blindness in developed countries for people older than 60 years, and accounts for nearly 9% of all blindness worldwide. It is projected that 196 million people will suffer from AMD by the year 2020 (Wong et al. 2014).

AMD progresses in either a dry or a wet stage. In its dry stage, cellular debris called drusen begin to accumulate between the choroid and the retina, causing a patients vision to deteriorate. Progression of the disease can ultimately lead to retinal detachment and complete loss of vision. There is currently no treatment for dry form AMD. In the wet form, AMD is progressed by vascular endothelial growth factors, which causes abnormal blood vessel growth in the macula (i.e., the center of the retina), which is responsible for central vision (see Figure 3-1). If left untreated, blood vessels in the macula can leak or burst, causing damage to the retina. As a result, patients central vision deteriorates, ultimately leading to blindness.

The current gold-standard treatment for AMD requires delivering drugs to the vitreous (i.e. interior of the eye) via intravitreal injection, thus enabling more efficient

posterior segment targeting for treatment. Intraocular injections of anti-vascular endothelial growth factor drugs such as bevacizumab (Avastin, Genentech, Oceanside, CA) or ranibizumab (Lucentis, Genentech) are used to help slow, or in some cases halt, the growth of abnormal blood vessels in the macula. This method of delivery provides excellent posterior segment targeting by delivering drugs directly to the macula region for treatment. However, due to the current half-life of existing drugs, monthly or bi-monthly treatments are required, putting a significant burden on the medical system. Furthermore, patients require treatment for the remainder of their lives if they wish to preserve their vision, with causing patient compliance to become an issue.

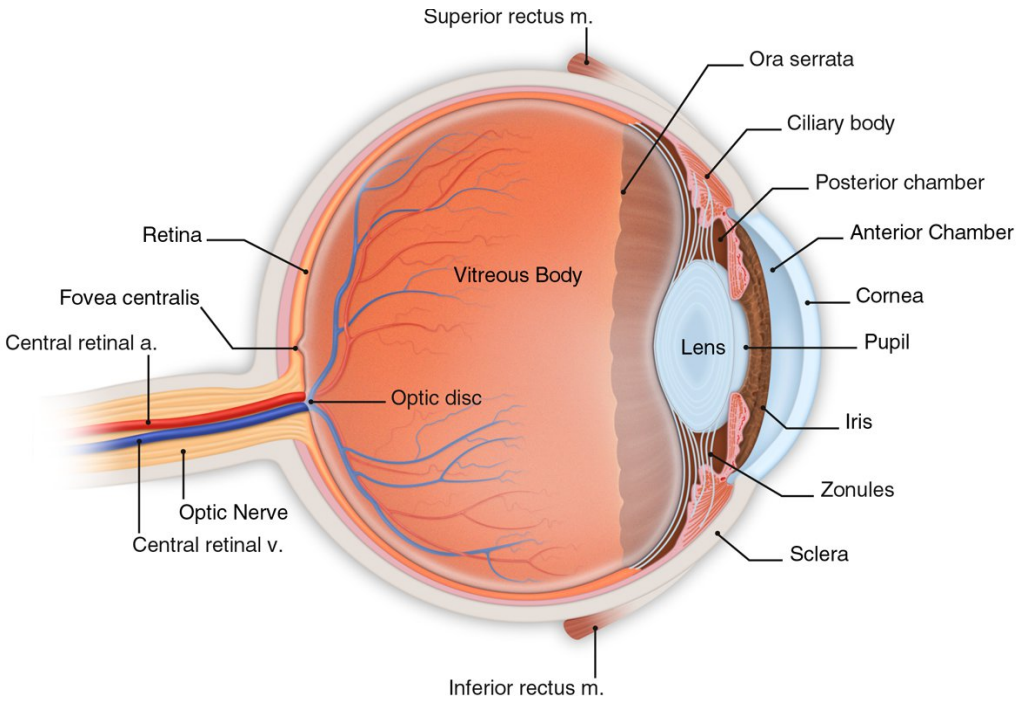

Figure 3-1. Schematic of the eye (www.totaleye.org).

3.1.2. Routes for Ocular Drug Delivery

A number of current and emerging drug therapies offer means for slowing the progression of leading ocular diseases like AMD, diabetic retinopathy (DR), and glaucoma, thus providing the possibility for preservation of sight in those so afflicted. However, the treatment of these diseases is nonetheless hampered by limitations inherent to the techniques currently available for the delivery of such therapies (Urtti 2006).

For example, the opportunity for delivery via systemic approaches (e.g., oral formulations or parenteral injections) is largely precluded by lack of specificity, which results in undesirable side effects and systemic toxicity (Gaudana et al. 2009). Topical delivery (e.g., via eye drops) allows for better targeting and, as such, is used widely for many indications (A. Patel 2013). However, this approach is highly inefficient (i.e., drug bioavailability < 3% in many cases), and is also subject to poor patient compliance, due in part to the required frequency of application (Osterberg and Blaschke 2005). Moreover, the epithelial transport barrier, conjunctival clearance, and other mechanisms prevent the delivery of sufficient concentrations to the back of the eye (e.g., the retina), thus limiting utility for treatment of posterior segment diseases (e.g., AMD and DR) (Järvinen, Järvinen, and Urtti 1995). Finally, while posterior segment targeting can be improved through use of intravitreal injection, this approach is associated with a small, but non-negligible risk for potentially devastating complications. Specifically, due to the compromising of the various barriers of the eye during needle insertion through the sclera into the vitreous (i.e., the gelatinous mass in the middle of the eye), complications could include infection, intraocular inflammation, and retinal detachment (Falavarjani and

Nguyen 2013; Shima et al. 2008). Moreover, when coupled with the need for frequently recurring treatment by trained medical personnel, the use of intravitreal injection imposes a significant burden on the healthcare system (Wong et al. 2014; Varma et al. 2011). Taken together, this demonstrates the need for development of a safer, simpler, and more efficacious means for ocular drug delivery.

Motivated by the significance of this need, and its attendant market potential, a wide variety of alternative targeted delivery approaches are currently being explored by the academic and industrial research communities. Typically, these approaches seek to circumvent physiological transport barriers (e.g., via permeability enhancers or nanoparticle formulations (Gan et al. 2013)) and/or achieve sustained delivery (e.g., via drug-eluting contact lenses (Joseph B. Ciolino et al. 2014; J. B. Ciolino et al. 2009), or implantable reservoirs (Lo et al. 2009; Lo et al. 2009; Gensler et al. 2012)). However, while many of these approaches show potential for enhancing safety, simplicity, or efficacy, none address all requirements simultaneously.

3.1.3. Microneedles for Drug Delivery

Microneedles (MNs) were first developed in the 1990s as a means for circumventing the epithelium and outer stratum corneum layer of the skin for transdermal drug delivery. The intent of MNs was to replace the need for painful parenteral injections with standard hypodermic needles by creating micron-scale perforations in the skin that allow active transport pathways for drugs to be delivered sub-surface. It was not until technological manufacturing advances in the micromachining and semiconductor

industry were made that the fabrication of such small devices became possible. Since their emergence, MN devices and systems have been fabricated using a wide variety of methods and materials for numerous biological applications.

The most common approach to using MNs for drug delivery has focused on the development of solid MNs for passive delivery. Solid MNs are fabricated with solid shanks, as opposed to hollow lumens shanks that are more commonly used for delivery applications (e.g., hypodermic needles used to infuse or draw fluids). These types of devices are typically fabricated from Si or metal, but can also be developed from various polymers. Multiple delivery techniques exist for solid MNs, and vary by application; however, all methods work on the principle of using the MN to bypass solute transport limiting epithilium layers by penetrating into tissue, thereby creating active transport pathways for drug diffusion (Prausnitz 2004). The first method is referred to as "poke with patch" and uses MNs to create perforations in the tissue surface, followed by the application of a drug patch or solution. Drugs are then allowed to diffuse through the punctured tissue by means of passive delivery, or are assisted by iontophoresis in the presence of an electric field. Another common approach is the "coat and poke" method, which utilizes a process for coating solid MNs with a drug formulation. In this approach, the MN serves as a means to penetrate into the tissue and as a carrier to deliver the drug to the sub-surface. Fast-dissolving coatings used for such devices rely on passive diffusive transport to release and deliver the drugs off the MN shank upon insertion into hydrated tissues.

The first MNs developed for transdermal drug delivery were fabricated from Si using DRIE techniques (Henry et al. 1998). As shown in Figure 3-2, out-of-plane arrays of 150 μm length solid MNs were developed. MN penetration studies utilized excised human skin to demonstrate successful MNs penetration and a four orders of magnitude increase in calcein permeability through the tissue after microneedling.

The less commonly used MN design is based on hollow geometry devices, and utilizes lumens for active fluidic transport, thereby making infusion or withdrawal possible. Hollow MNs have been fabricated primarily from silicon and glass, but have also been developed using metals. For example, hollow metal MNs for insulin delivery have been developed using a combination of micromolding and laser machining techniques (S.P. Davis et al. 2005). As shown in Figure 3-3, these hollow MNs were

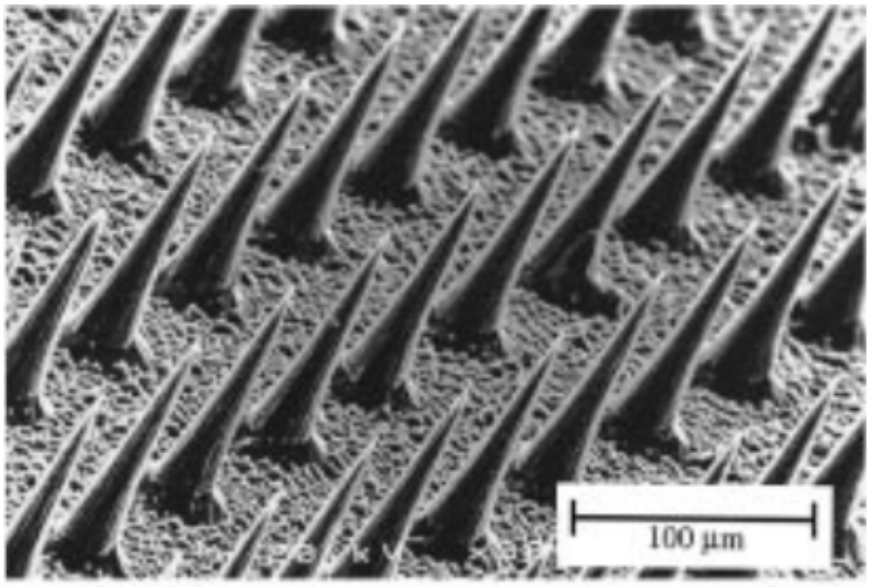

Figure 3-2. First reported microfabricated solid MNs for transdermal drug delivery (Henry et al. 1998).

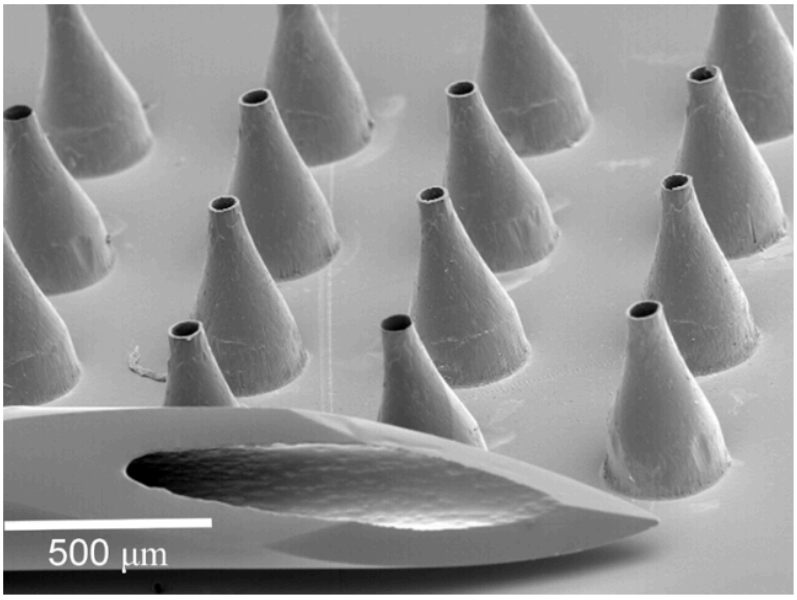

Figure 3-3. Scanning electron micrograph of microfabricated hollow MNs for transdermal drug delivery (S.P. Davis et al. 2005).

formed in arrays from electrodeposited nickel. Studies showed that MNs were capable of penetrating into the skin of human subjects in a minimally invasive way, and also proved its ability to deliver insulin to diabetic rats successfully. Although these devices allowed for one means of transdermal delivery, nickel is a known skin irritant, thereby limiting its ability for translation into clinical use.

3.1.4. Microneedles for Ocular Delivery

MNs offer significant promise in regards to ocular drug delivery, due in large part to their diminutive size, which allows for penetration into, but not through the sclera or cornea (J Jiang et al. 2007; J Jiang et al. 2009; S. R. Patel et al. 2011; Kim, Edelhauser,

and Prausnitz 2014; Kim et al. 2014). In doing so, this provides a precise and minimally-invasive means for depositing drugs within such tissues, which can then be transported to the disease site via diffusion. As such, MNs enable circumvention of the epithelial transport barrier and conjunctival clearance mechanism, while also minimizing potential for retinal damage. Moreover, the potential for simplified application afforded by MNs may also reduce the demand upon medical personnel. This, therefore, could provide an opportunity for a near-optimal balance of safety, simplicity, and efficacy.

While MNs based on both passive (J Jiang et al. 2007; Kim et al. 2014) and active (J Jiang et al. 2009; SR Patel et al. 2011; Kim, Edelhauser, and Prausnitz 2014) delivery approaches have been recently reported, the former may ultimately prove more advantageous for routine clinical use. This is due to the simplified nature of such devices, which typically consist of arrays of solid MNs with fast-dissolving drug coatings applied to the needle shanks. However, the potential for clinical translation of such devices may be ultimately constrained by their limited drug carrying capacity, since this could necessitate the use of prohibitively large arrays for delivery of therapeutically-relevant dosages.

During the past decade, academic institutions have begun researching the utility of MNs for delivering drugs to the eye in a minimally invasive manner. The first demonstration of this application was developed at Georgia Tech University by Professor Mark R. Prausnitz and his team of researchers, and utilized 200 μm wide, 50 μm thickness, and 750 μm length solid stainless steel MNs coated with fast-dissolving aqueous drug formulations to passively deliver drugs via intrascleral and intracorneal

routes (J Jiang et al. 2007). Solid MNs (Figure 3-4) were fabricated by laser micromachining stainless steel sheets, followed by electrochemical cleaning and dip coating of a model drug. Their delivery studies showed that coated MNs could be used to deliver drugs within the sclera tissue within 30 seconds of insertion, and that delivery efficiencies to the anterior chamber (i.e., the back of the eye) were 60 times greater than those achieved using topically administered drugs. Furthermore, their results determined there was no measurable inflammatory response after penetrating uncoated MNs within the cornea of a New Zealand white rabbit *in vivo*, and that the penetration site had healed within 3 hours of MN insertion.

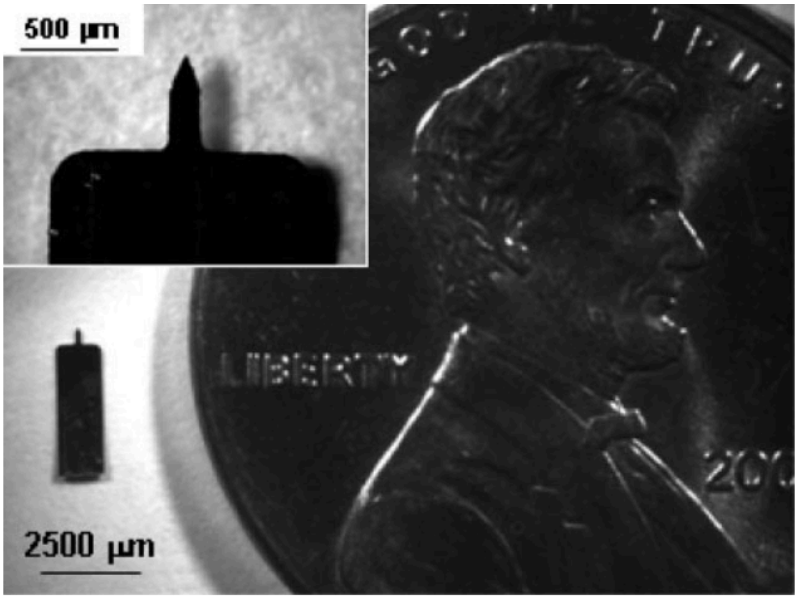

Figure 3-4. Digital photographs of laser micromachined solid stainless steel MNs for intrascleral and intracorneal drug delivery (J Jiang et al. 2007).

The first demonstrated use of hollow MNs to deliver drugs to the eye emerged in 2009 by J. Jiang et al.. In their study, 800 - 1000 μm length hollow glass MNs were fabricated from borosilicate micropipette tubes using a micropipette puller. The MN tips were then ground to a 20° tip angle using a glass grinder and subsequently cleaned for use (Figure 3-5). Results showed that individual hollow MNs were able to successfully infuse 10 - 35 μl of fluid into the sclera using minimally invasive technique. They found that delivery efficiencies improved using partial retraction techniques, and that scleral thickness and infusion pressure had insignificant effects on the fluid delivery.

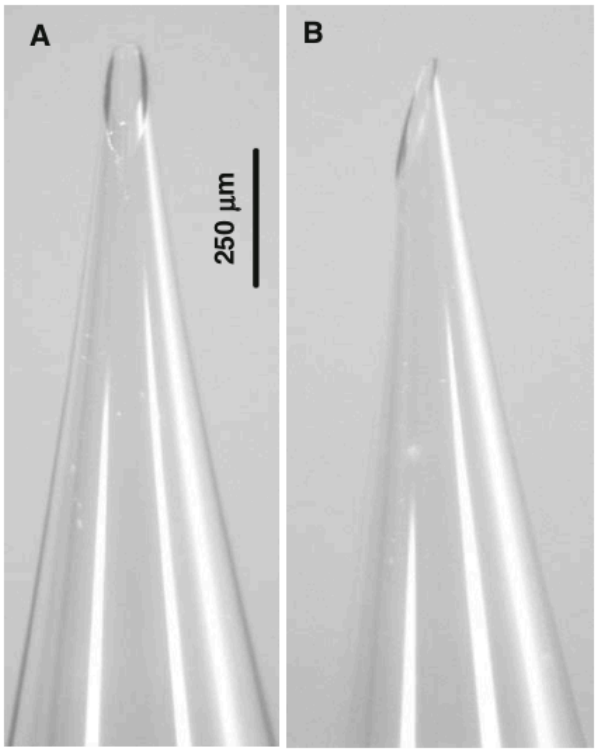

Figure 3-5. Digital photographs of hollow glass MNs for intrascleral drug delivery (J Jiang et al. 2009): a) Front view; b) Side view.

In 2011, S. R. Patel et al. demonstrated the use of similar geometry hollow glass MNs to successfully deliver both micro- and nanoparticles into the suprachoroidal space of rabbit, pig, and human eyes. Delivery studies showed successful volumes up to 35 µl using infusion pressures of 250 to 300 kPa. This study provided another example for delivering drugs to the back of the eye in a minimally invasive method by using MNs. Similar studies of delivering to the suprachoroidal space followed in 2012, using hollow metal MNs fabricated from 33-gauge needles (Figure 3-6) (S. R. Patel et al. 2012). MNs in these studies were shown to be successful in delivering 40 and 250 kDa fluorescent molecules as well as 20 nm to 10 µm diameter polymeric particles to the suprachoroidal space for posterior segment treatment.

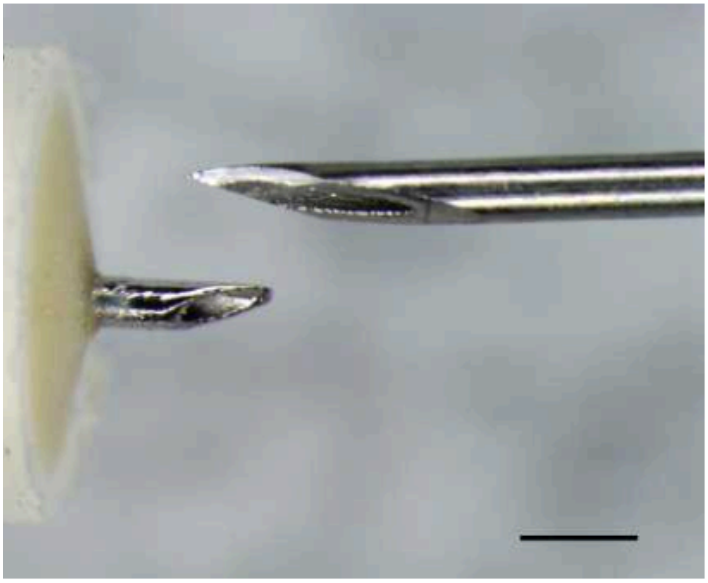

Figure 3-6. Digital photograph of hollow stainless steel MN for drug delivery to the suprachoroidal space. Scale bar represents 500 µm (S. R. Patel et al. 2012).

While both solid and hollow MN-based design approaches provide a means for successful posterior segment ocular delivery, devices based on passive delivery may ultimately prove more advantageous for routine clinical use, due to lower complexity and cost, and especially due to the disposable nature of such devices. While stainless steel based MNs provide a means for passive delivery and enhanced safety relative to silicon or glass devices, current fabrication techniques using laser micromachining has limited potential for batch fabrication and scalability. Since these devices are intended for single use delivery, scalability for low-cost fabrication becomes critically important. Furthermore, the potential for clinical translation will be constrained by the limited drug loading capacity of devices demonstrated to date, since this necessitates use of excessively large MN arrays to deliver therapeutically-relevant dosages.

3.1.5. Scope of this Work

Herein, we report the development of titanium-based MNs that seek to address the current limitations of MNs used to treat posterior segment ocular diseases. The key novelty of these devices lies in their use of through-thickness fenestrations (i.e., windows), which seek to increase drug carrying capacity relative to solid MNs. Using our novel titanium deep reactive ion etching (Ti DRIE) process, we show that fenestrated Ti MNs with complex geometries can be fabricated utilizing standard semiconductor processing techniques which allow for low-cost manufacturing for scalability. Furthermore, using finite element analysis and mechanical testing methods, we show that these devices possess sufficient stiffness for reliable insertion, and that the primary mode

of failure is by graceful plasticity-based deformation, thereby improving safety relative to conventional Si or glass devices. Finally, we show that these devices can increase drug carrying capacity up to five-fold relative to solid MNs of comparable size, as well as can enhance sub-surface drug deposition in an excised rabbit cornea model. As such, our studies begin to demonstrate the potential that is embodied in fenestrated Ti MNs for ocular drug delivery.

3.2. Materials and Methods

3.2.1. Materials

For this study, Ti foils was selected as the substrate of choice for its compatability with the through-etching capability of the Ti DRIE process. Specifically, MNs were designed to be fabricated from 50 μm thick Grade 1 Commercially Pure (CP) Ti foils (ground finish) (Fine Metals Co., Ashland, VA)) based on its ability to provide a mechanically robust device for insertion into the cornea or sclera while maintaining a diminutive thickness to minimize trauma to the surrounding tissue.

Due to the inherent bow of the Ti foils and strict planarity requirements for successful lithography and micromachining, a method for mounting and adhering the Ti substrates to a flat carrier chip was necessary. To enable micromachining of Ti foils, substrates were mounted to a single sided polished silicon carrier chip using double sided thermally conductive adhesive tape (9882, 3M, St. Paul, MN). Details regarding the substrate mounting process are outlined in Appendix A.

3.2.2. Microneedle Design

The fenestrated Ti MNs produced in this study were designed for passive intracorneal and intrascleral delivery within an *ex vivo* rabbit model via diffusive transport from a fast-dissolving coating. As shown in Figure 3-7, MNs were designed with complex through-thickness fenestrations that serve as drug reservoirs, while a trussed structure was selected to maximize carrying capacity and maintain sufficient stiffness for insertion. Estimates based upon assumptions of complete fenestration filling and 1 μm global coating thickness suggested that these fenestrations could increase carrying capacity up to five-fold relative to solid MNs of identical shank dimensions (Table 3-1).

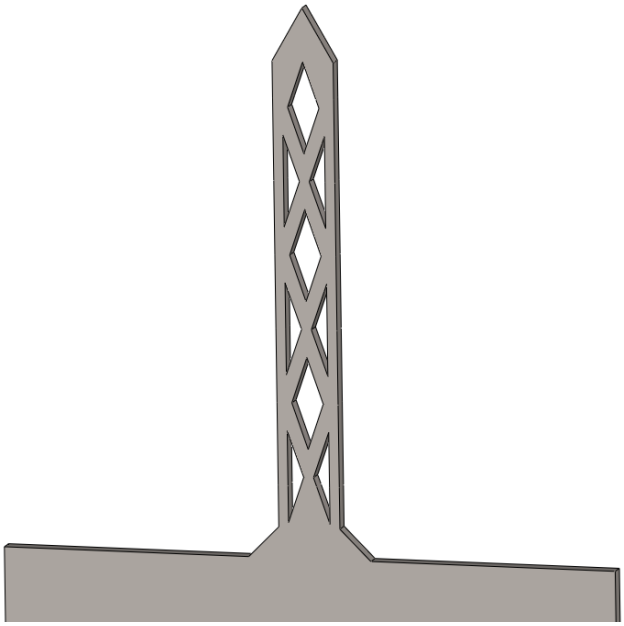

Figure 3-7. Schematic of the fenestrated MN design concept. The pictured MN has dimensions of 200 μm width, 50 μm thickness, and 1500 μm length. All fenestrations project through the thickness of the needle shank.

Table 3-1. Estimated increase in drug carrying capacity for fenestrated Ti MNs relative to solid MNs of identical shank dimensions. Estimates are based upon assumption of complete fenestration filling and 1 μm global coating thickness.

		MN width [μm]			
		50	100	150	200
MN length [μm]	500	184%	210%	332%	412%
	1000	221%	247%	329%	518%
	1500	238%	293%	374%	526%

The fenestrated MNs were designed with widths of 50, 100, 150, and 200 μm, a fixed thickness of 50 μm, lengths of 500, 1000, and 1500 μm, and a fixed needle tip angle of 60°. The dimensions of the fenestrations ranged from 12.5 μm to 75 μm along their long axes, scaling with increasing MN width. This design parameter space allowed for a total of 12 unique fenestrated MN geometries to be studied. Since optimal designs for the intended applications have yet to be defined, the given variation of these parameters was reflective of the desire to eventually determine the most favorable combination that ensures reliable insertion, minimized trauma, and maximum delivery efficiency. As shown in Figure 3-8, solid MNs of identical shank dimensions were also designed to serve as controls.

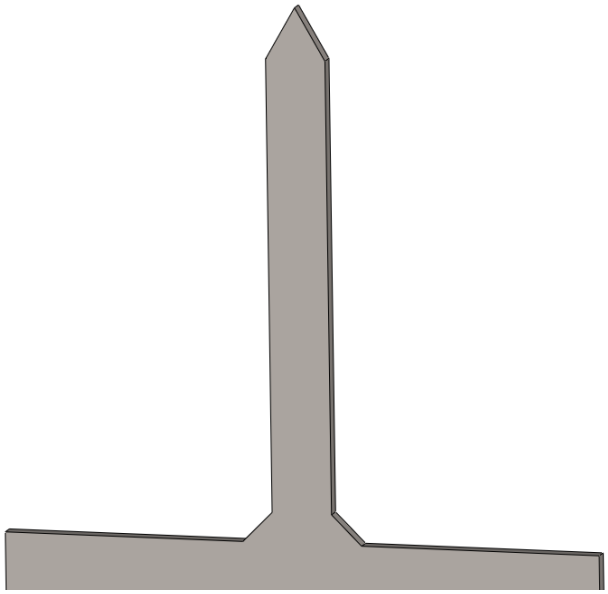

Figure 3-8. Schematic of the solid MN design concept. The pictured MN has dimensions of 200 μm width, 50 μm thickness, and 1500 μm length.

3.2.3. Finite Element Analysis Simulation

Finite element analyses (FEA) were performed for all MN design variants to evaluate buckling performance, since this was expected to be the primary failure of mode during insertion. The simulations were performed using a commercial FEA package (SolidWorks Simulation, Waltham, MA). Relevant material properties used for the Ti included: Young's modulus = 103 GPa, Poisson's ratio = 0.34, density = 4.51 g/cm^3, and yield strength = 170 MPa (Gerhard, Boyer, and Collings 1994). Analyses for both fixed-free and fixed-pinned end conditions were performed, since our earlier studies of other needle-based microdevices suggested that these would be most appropriate (ER Parker et al. 2007; McCarthy, Otto, and Rao 2011). Meshing varied widely amongst the designs,

due to the large dimensional space explored; however, a minimum of 5E4 brick elements and 9E4 nodes was used for all simulations.

3.2.4. Fabrication

All MNs were fabricated using 50 μm thick Grade 1 CP Ti foils. Prior to fabrication, the foils were cleaned using ultrasonic agitation in sequential baths of acetone, isopropanol, and deionized water, followed by drying with ultrahigh purity nitrogen. As illustrated in Figure 3-9, 3 μm thick SiO_2 etch masks were deposited using high density plasma enhanced chemical vapor deposition (VLR, Unaxis, St. Petersburg, FL; Process conditions: 15 mT chamber pressure, 400 W ICP source power, 5 W substrate power, 5.9 sccm 100% SiH_4, 20 sccm Ar, 10 sccm O_2, and 100°C lower electrode temperature). Following deposition, hexamethyldisilazane (HMDS) was dispensed and spun on the substrates, followed by photoresist spin-coating (SPR220-7.0, Shipley). Photoresist patterning of the MN designs was performed using a patterned quartz photomask and hard contact lithography (MA6 Mask Aligner, SUSS MicroTec, Germany). This was followed by mask oxide dry etching (E640-ICP, Panasonic Factory Solutions, Osaka, Japan; Process conditions: 3.75 mT chamber pressure, 900 W ICP source power, 200 W substrate power, 40 sccm CHF_3). Photoresist was then removed from the substrates using solvent cleaning followed by a 1 min O_2 plasma descum (Technics/PE-IIA; Process conditions: 100 W, 300 mT) to ensure all residual photoresist was removed from the substrate. Anisotropic through-etching of the underlying Ti was then performed using Ti DRIE (E640-ICP; Process conditions: 15 mT chamber pressure, 400 W ICP source power, 100 W substrate power, 100 sccm Cl_2, 5 sccm Ar, and 1 sccm

O_2). Finally, the residual etch mask was removed by dry etching (E640-ICP; Process conditions: 7.5 mT chamber pressure, 600 W ICP source power, 50 W substrate power, 50 sccm SF_6, 10 sccm Ar).

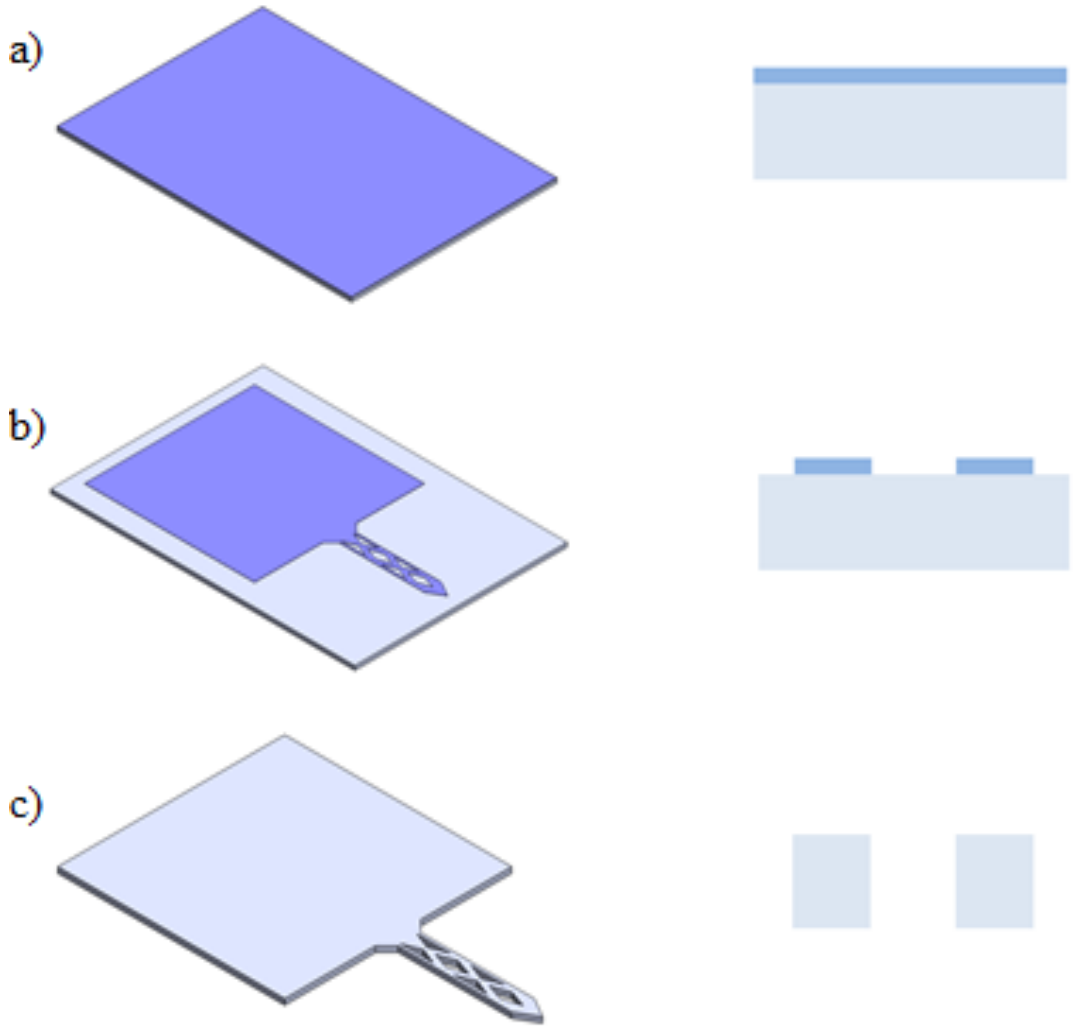

Figure 3-9. Fabrication process for fenestrated Ti MNs: a) PECVD-based deposition of 3 µm SiO_2 layer on 50 µm thick Ti foil; b) Photolithographic patterning and dry etching of SiO_2 etch mask; and c) Ti DRIE followed by mask removal via dry etching.

3.2.5. Coating

The coating formulations used in this work were derived from those reported in earlier studies (Gill and Prausnitz 2007b). Aqueous formulations were prepared using 15% polyvinylpyrrolidone (PVP, M_w = 1,300 kDa, Sigma Aldrich, St. Louis, MO), and 1% Rhodamine B (M_w = 479 Da, Sigma Aldrich) (all w/v %), since these were shown to provide a good balance of viscosity and wettability, while also allowing complete dissolution in water within 15 s. In these formulations, PVP served as a viscosity enhancer, while Rhodamine B served as a model small molecule drug. The Rhodamine also provided means for characterizing coating performance via fluorescence microscopy.

The MNs were manually dip-coated while observed under a high magnification camera using a custom-built apparatus. The coating apparatus consisted of a manual syringe (not pictured) connected to a fixed length of 1/16" outer diameter x 0.020" inner diameter liquid chromatography (LC) PEEK tubing. Adjacent to the tubing was a manually-driven microactuator stage with a single MN affixed using double-sided adhesive tape. The coating process consisted of dispensing a fresh droplet of formulation, manually inserting the MN into the droplet, and then manually withdrawing the MN at a fixed rate. A 3 minute interval was used between coats to allow for sufficient drying. Prior to each coat, and a new droplet of formulation was dispensed. Coating process development studies were performed to define optimal conditions for uniform MN coating and fenestration filling, while minimizing the potential for excess coating of the MN shank, which could lead to shear-induced loss of coating at the surface upon

insertion into tissue. Studies were performed to better understand the effects the withdraw speed and number of coats had on coating quality.

3.3. Device Characterization

3.3.1. Mechanical Testing

The buckling behavior of the MNs was assessed by longitudinal uniaxial compression under displacement-controlled conditions using a nanoindenter (TI 950 TriboIndenter, Hysitron, Minneapolis, MN) equipped with a 100 μm diameter flat diamond tip probe. The critical buckling load ($P_{critical}$) for each design variant was extracted from the recorded load-displacement data. A minimum of 8 MNs were tested for each design variant.

3.3.2. Coating Evaluation

The uniformity of the MN coatings was characterized by fluorescence microscopy (Leica DM2000, Leica Microsystems, Buffalo Grove, IL), and the drug carrying capacity was quantified using spectrophotometry (Cary 50 UV-Vis, Varian, Santa Clara, CA). For the latter, individual MNs were first sonicated in DI water for 1 min to dissolve the coating. The Rhodamine B intensity in the eluent was then measured and converted to a mass loading using a previously developed calibration curve from a stock solution. A minimum of 6 MNs were measured for each design variant.

3.3.3. Delivery Characterization

Qualitative characterization of drug delivery from the coated MNs was performed using excised cornea from a New Zealand white rabbit (Sierra Medical for Science, Whittier, CA). Prior to testing, the tissue preparations were submerged in phosphate buffered saline (PBS, Fisher BioReagents, Hampton, NH) for 5 min. They were then removed, blotted dry to remove excess liquid on the surface, and mounted on a hemispherical block with radius of curvature approximating that of a rabbit eye. Coated MNs were manually inserted and allowed to remain in place for 1 min to provide sufficient time for the coatings to dissolve. The MNs were then removed, followed by sectioning of the corneas near the insertion sites using a cryostat (Tissue Tek II 4553 Cryostat, Ames Miles). The tissue sections were then examined using fluorescence microscopy.

3.4. Results and Discussion

3.4.1. Fabrication

Figure 3-10 shows a representative scanning electron micrograph of a fenestrated Ti MN with 200 μm width, 50 μm thickness, and 1500 μm length. Faithful reproduction of the fenestration geometry is observed. Similarly faithful reproduction of the fenestrations was observed for all other MN design variants. This demonstrates the unique capability afforded by Ti DRIE for realization of complex, high-aspect-ratio Ti-based microdevice structures that would be difficult, if not impossible, to achieve with

other metal micromachining methods (e.g., laser micromachining, microelectrodischarge machining, ultraprecision CNC, wet etching, 3-D printing, etc.).

Figure 3-11 illustrates the size of a representative Ti MN (200 μm width, 50 μm thickness, and 1500 μm length) relative to a conventional 26 gauge hypodermic needle. The diminutive nature of the fenestrated MN suggests potential for reduced tissue trauma and patient discomfort relative to the 26 gauge needle, a size commonly used for intravitreal injection. Moreover, the short length of the MN is intended to ensure penetration into, but not through sclera or cornea, thus reducing potential for infection and retinal detachment. Figure 3-12 shows a representative scanning electron micrograph of a solid Ti MN with dimensions 200 μm width, 50 μm thickness, and 1000 μm length that was used as a control for device characterization discussed in the next section.

a)

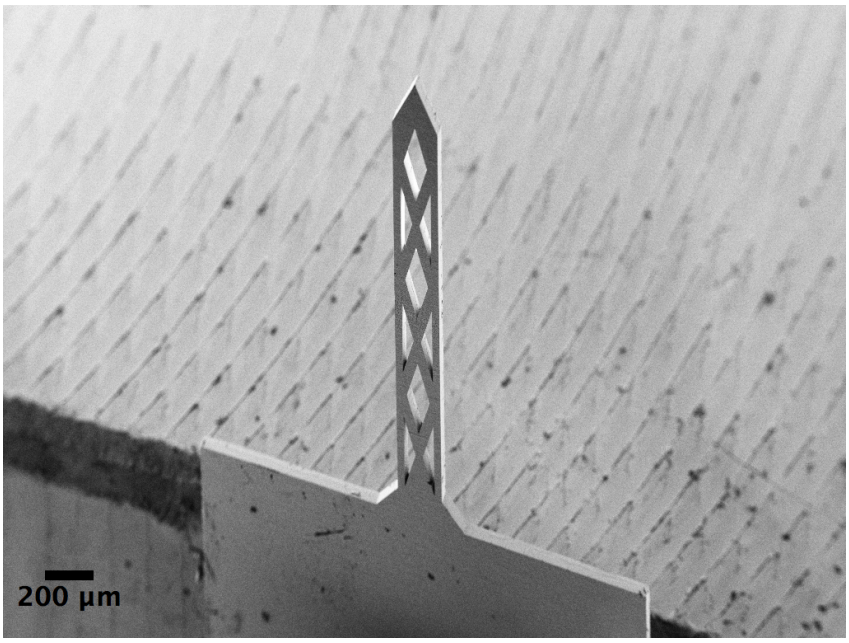

b)

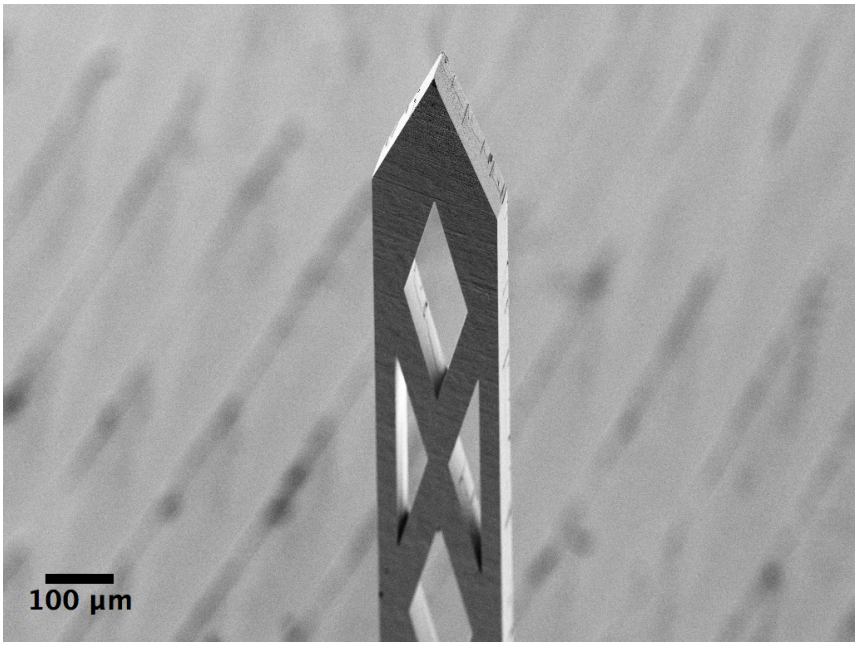

Figure 3-10. Scanning electron micrographs of fenestrated Ti MNs fabricated using Ti DRIE (200 µm width, 50 µm thickness, and 1500 µm length): a) Low magnification; b) High magnification.

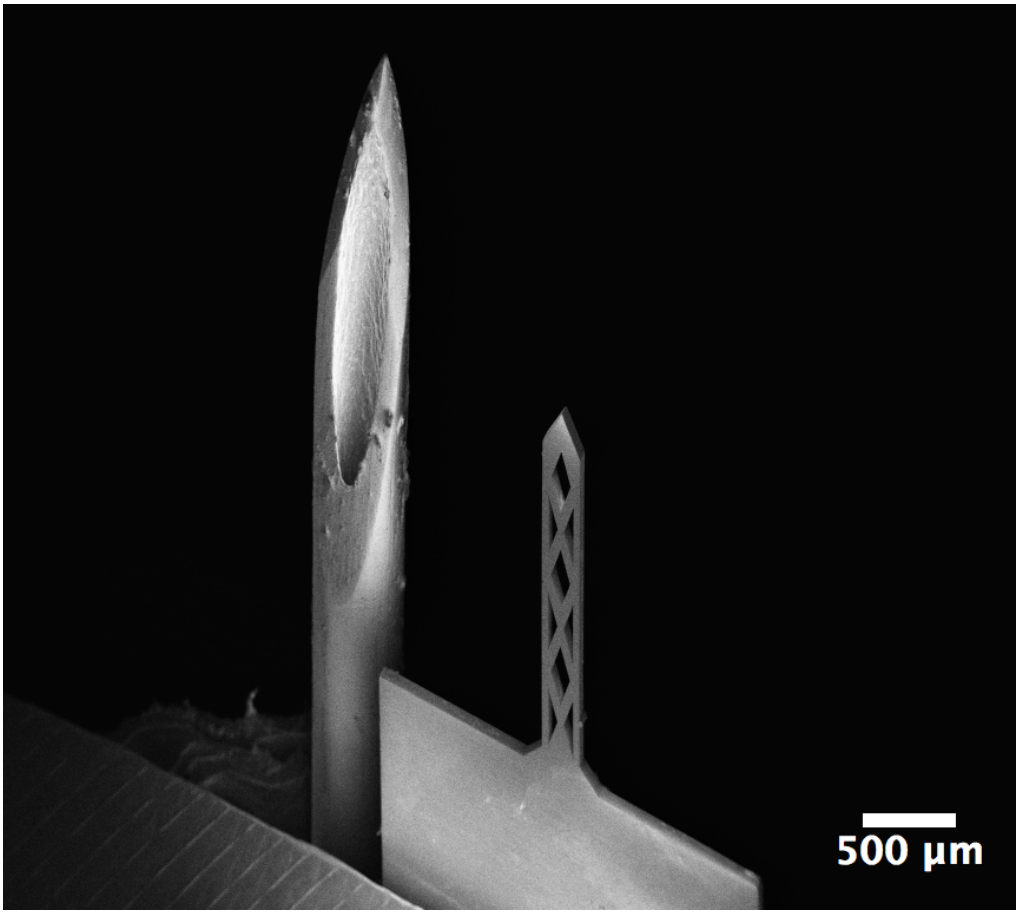

Figure 3-11. Scanning electron micrograph of fenestrated Ti MN (200 µm width, 50 µm thickness, and 1500 µm length) compared to 26 gauge hypodermic needle (464 µm outer diameter).

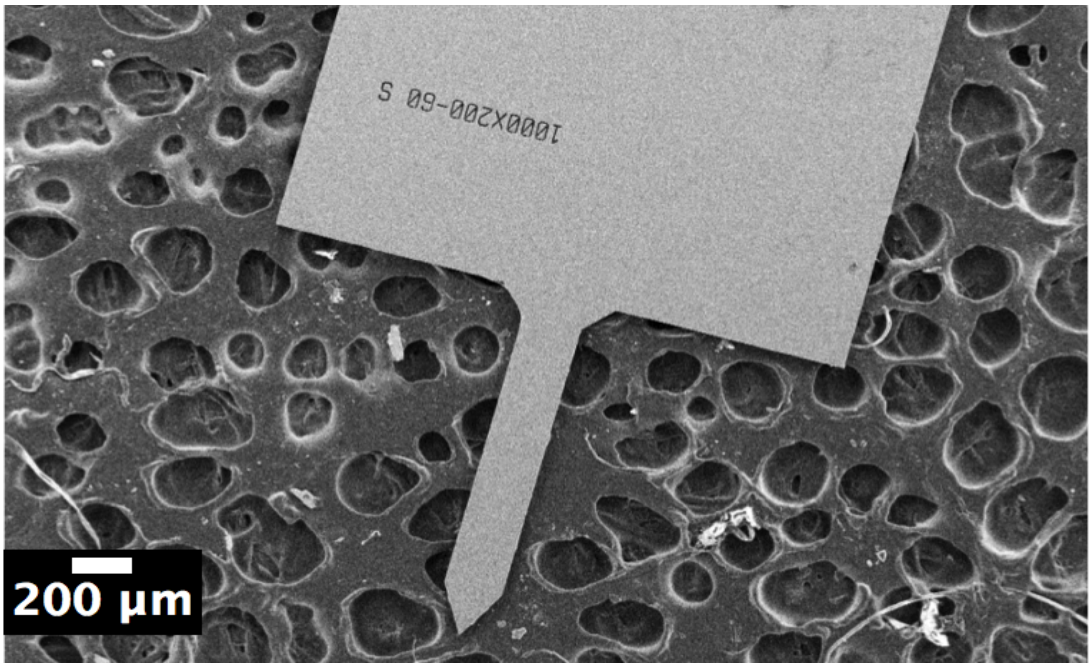

Figure 3-12. Scanning electron micrograph of solid Ti MN (200 µm width, 50 µm thickness, and 1000 µm length).

3.4.2. Mechanical Response

Figure 3-13 shows a representative scanning electron micrograph of a fenestrated Ti MN after mechanical testing (150 µm width, 50 µm thickness, and 1000 µm length). The graceful, plasticity-based failure mode is clearly evident. Similarly graceful failure was observed for all other MN design variants. This suggests that the use of Ti provides potential for greater safety and reliability than more conventional micromechanical materials (e.g., Si and SiO_2), since the intrinsic brittleness of these materials causes predisposition for catastrophic failure by fracture-based fragmentation. Moreover, the high elastic modulus and hardness of Ti suggests potential for more reliable insertion and reduced MN size relative to common durable and dissolvable polymers used for

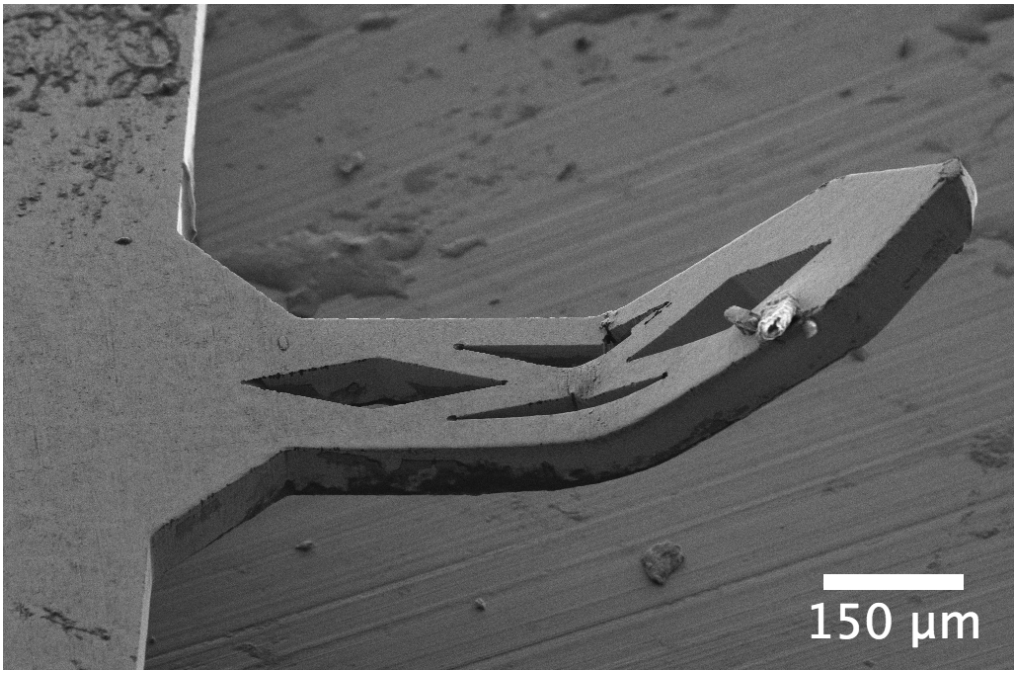

Figure 3-13. Scanning electron micrograph of buckled fenestrated Ti MN (150 μm width, 50 μm thickness, and 1000 μm length) after axial compression.

micromechanical applications (e.g., PMMA, polycarbonate, SU-8, PLLA, PLGA, etc.). Finally, the well-proven biocompatibility and corrosion resistance of Ti suggests potential for superiority to many metals used for micromechanical applications (e.g., Ni, Cu, Fe, etc.), as does its low cost relative to noble metals (e.g., Au, Pt, Pd, etc.). The latter is particularly important, since device disposability ultimately may be required for clinical and commercial feasibility.

Figure 3-14 shows a plot of the measured load-displacement data for select fenestrated Ti MNs. Figure 3-15 shows representative plots of FEA displacement for fenestrated Ti MNs. Figure 3-16 and Figure 3-17 show plots of the variation of critical buckling load as a function of MN length for the fenestrated Ti MNs with varying widths

and lengths and 50 µm thickness. For all MN lengths, the measured buckling loads were observed to fall within the bounds predicted by FEA for MNs with fixed-free and fixed-pinned end conditions. Similar responses were observed for solid MNs (see Figure F-1 and Figure F-2). This agreement validates the modeling, thus suggesting potential for further FEA-based design optimization in the future.

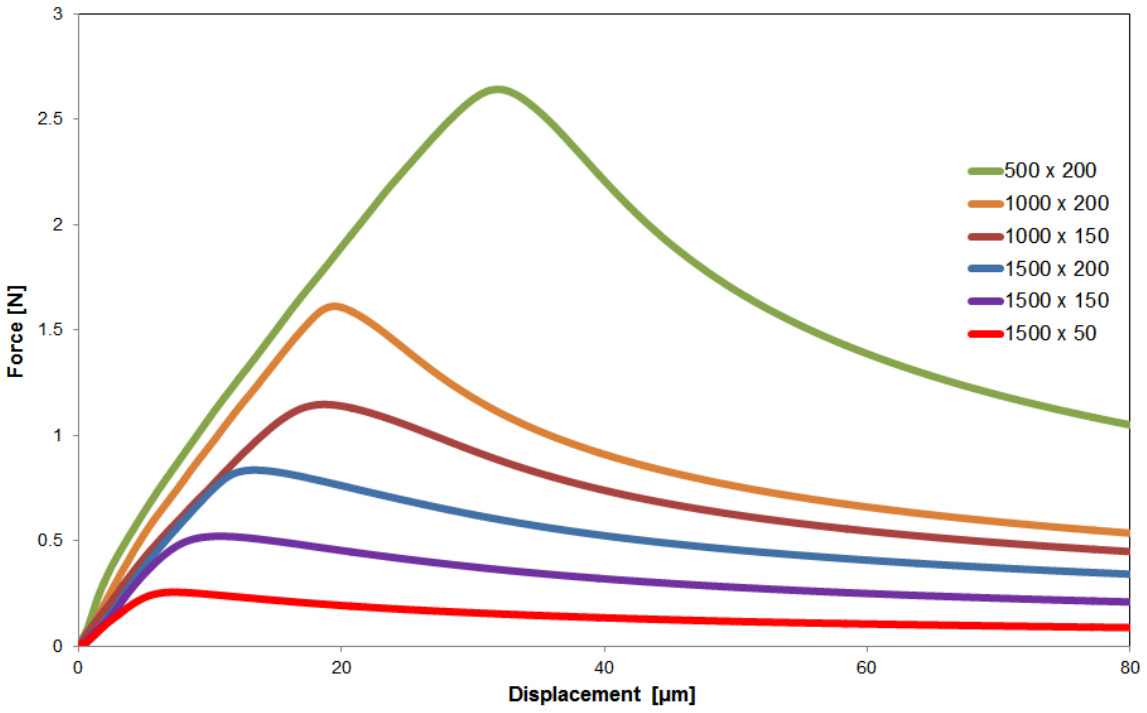

Figure 3-14. Plot of load-displacement data for select fenestrated Ti MNs under axial compression. Legend values correspond to data sets for MNs with given length and width in µm, and fixed 50 µm thickness.

a)

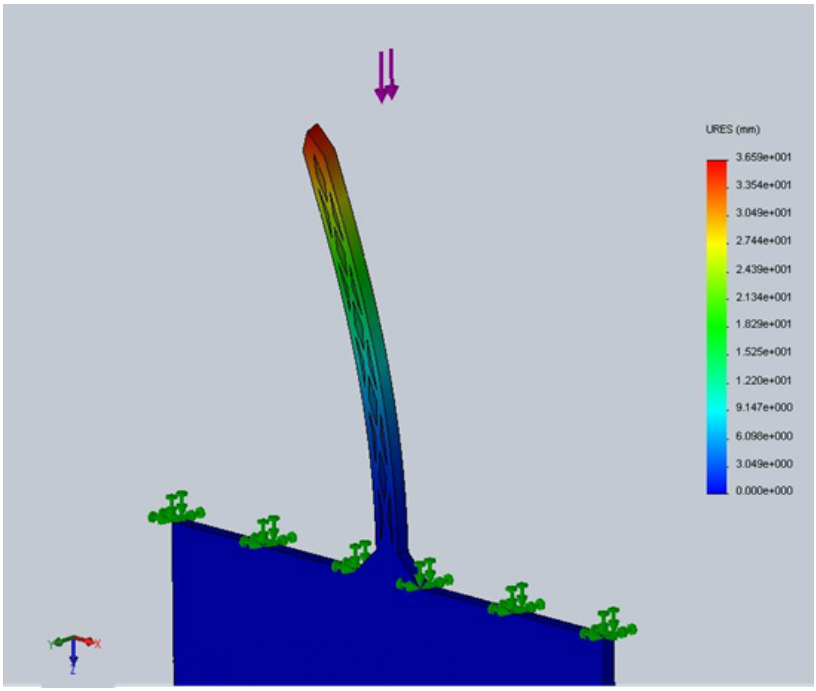

b)

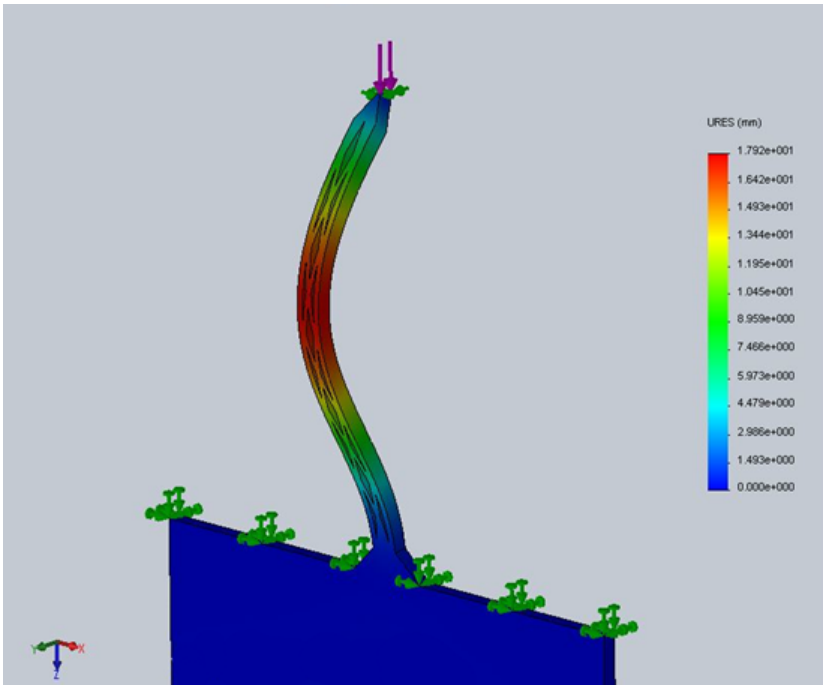

Figure 3-15. Representative plots of FEA displacement for fenestrated Ti MNs (100 µm width, 50 µm thickness, and 1500 µm length): a) Fixed-free mode; b) Fixed-pinned mode.

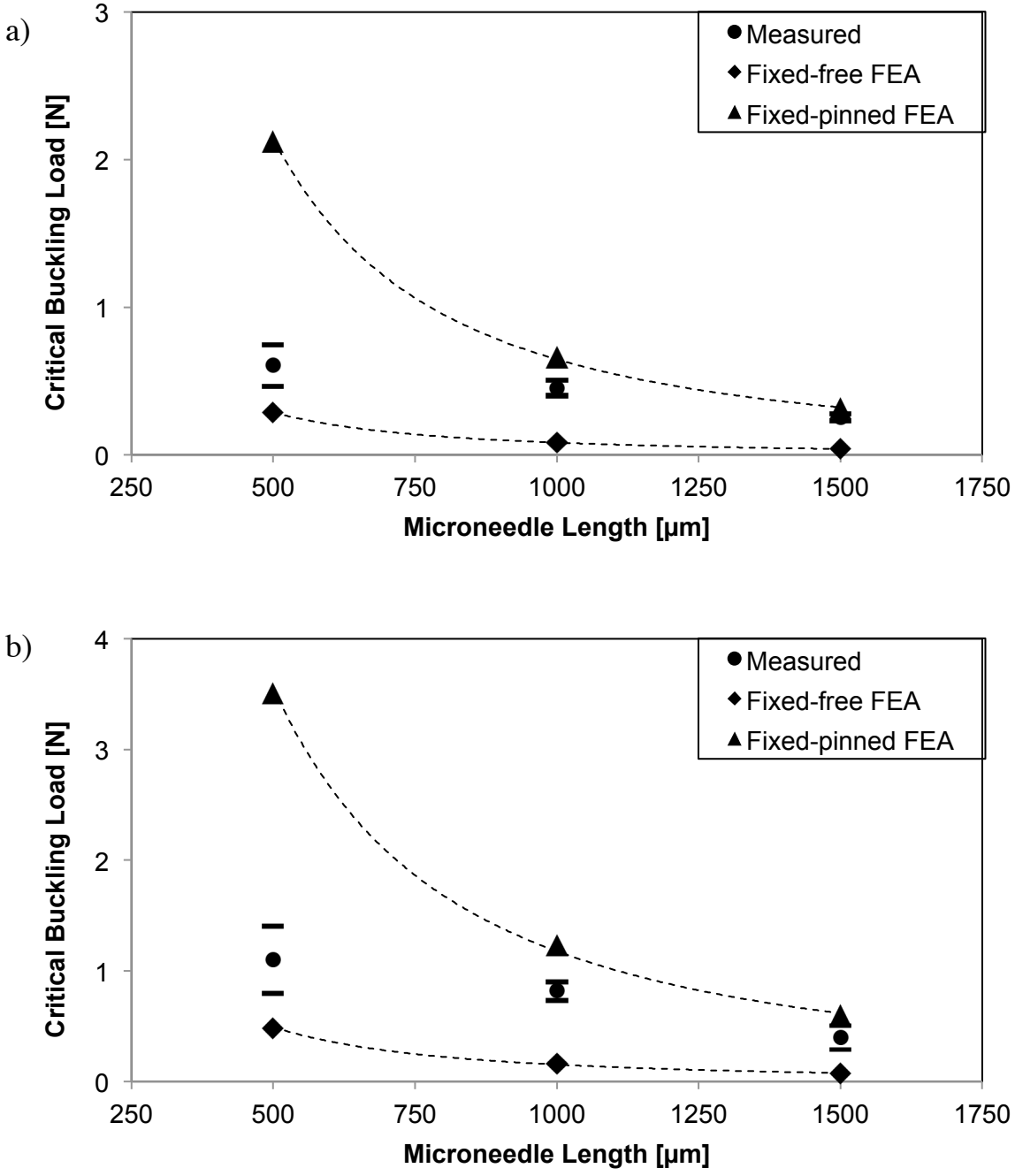

Figure 3-16. Measured and FEA-predicted critical buckling loads for fenestrated Ti MNs with varying μm width, 50 μm thickness, and 500 - 1500 μm lengths: a) 50 μm width; b) 100 μm width. Experimental data points represent average of 8 specimens.

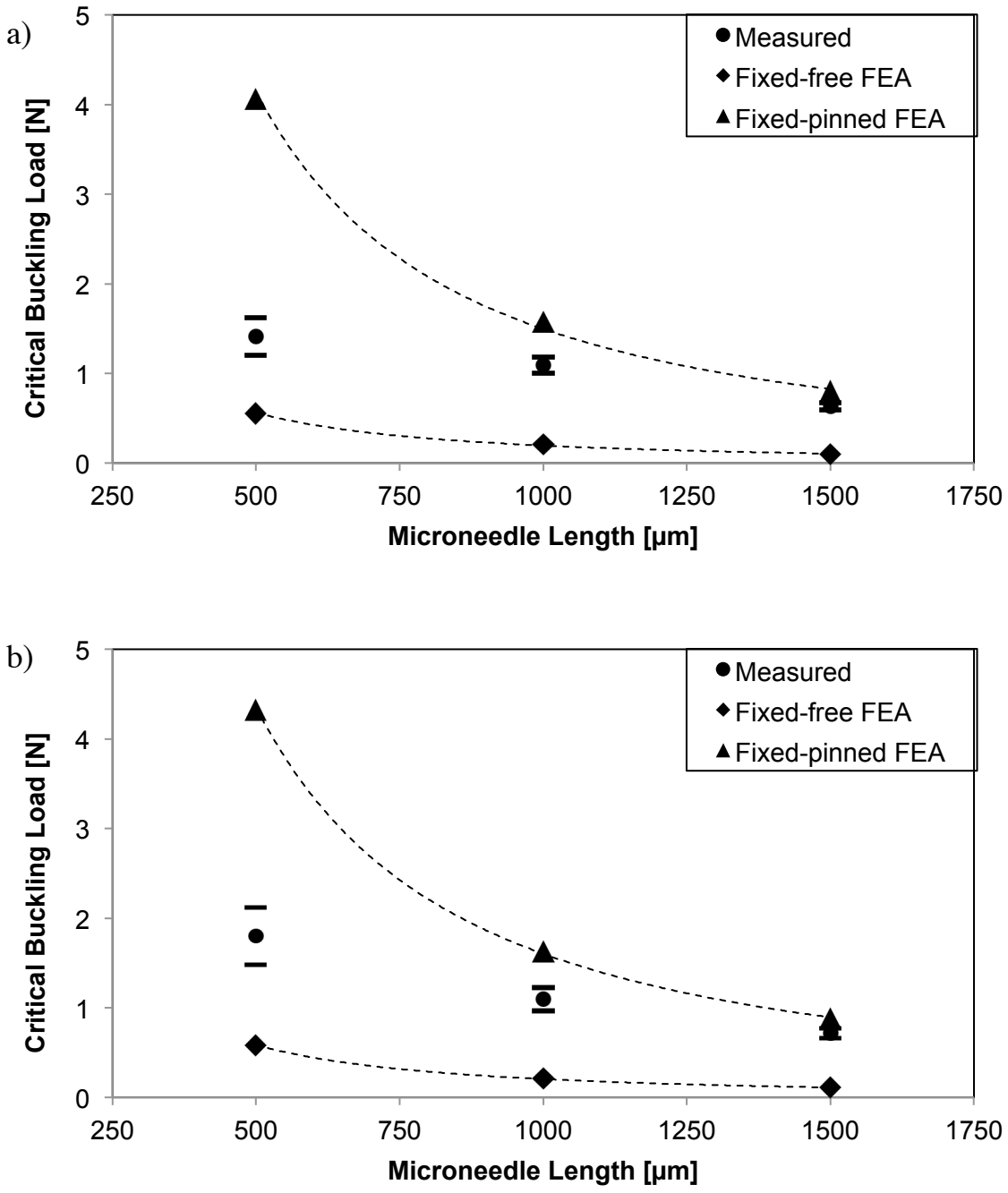

Figure 3-17. Measured and FEA-predicted critical buckling loads for fenestrated Ti MNs with varying μm width, 50 μm thickness, and 500 - 1500 μm lengths: a) 150 μm width; b) 200 μm width. Experimental data points represent average of 8 specimens.

It is important to note that the measured buckling loads for most of the MN design variants exceed the reported forces required for scleral and corneal insertion of conventional hypodermic needles in human cadaveric eyes (ranging from 0.29 N for 31 gauge needles, to 1.005 N for 18 gauge needles (Pulido, Zobitz, and An 2006; Matthews et al. 2014). This, therefore, suggests that most of the fenestrated Ti MN design variants developed in this study possess sufficient stiffness for intrascleral and intracorneal penetration *in vivo*, particularly since lower insertion loads are expected for MNs, due to their smaller cross section areas (Shawn P Davis et al. 2004).

3.4.3. Drug Carrying Capacity

MN coating evaluations determined coating uniformity and thickness were effected by withdraw speed and number of dip coats. Fenestrated and solid MNs were coated using withdraw rates from 0.1 - 2 mm/s. Higher withdraw speeds resulted thicker coatings on the MN shank, while lower rates produced thinner coatings. These findings were in good agreement with studies by others focused on the coating of similar geometry devices (Gill and Prausnitz 2007b). Optimal withdraw speeds for uniform MN coating and fenestration filling were determined to be 1.5 mm/s. Similar withdraw speed for solid MNs resulted in non-uniform coatings on the MN shank. Excess coatings resulted in dried formulations with “barrel” shapes along the center of the shank due to surface tension effects. These findings suggest that fenestrated MNs with through-etched features have potential for improved storage by serving as protective cavities for subsurface delivery. A withdraw speed of 0.15 mm/s was selected for solid MNs in order to produce uniform coatings while minimizing risk for shear-induced coating loss at the

surface upon insertion. To ensure consistency between coated devices, a new droplet of formulation was dispensed prior to each MN dip coat, and 3 minute intervals were allowed between coats to ensure sufficient coating dry time.

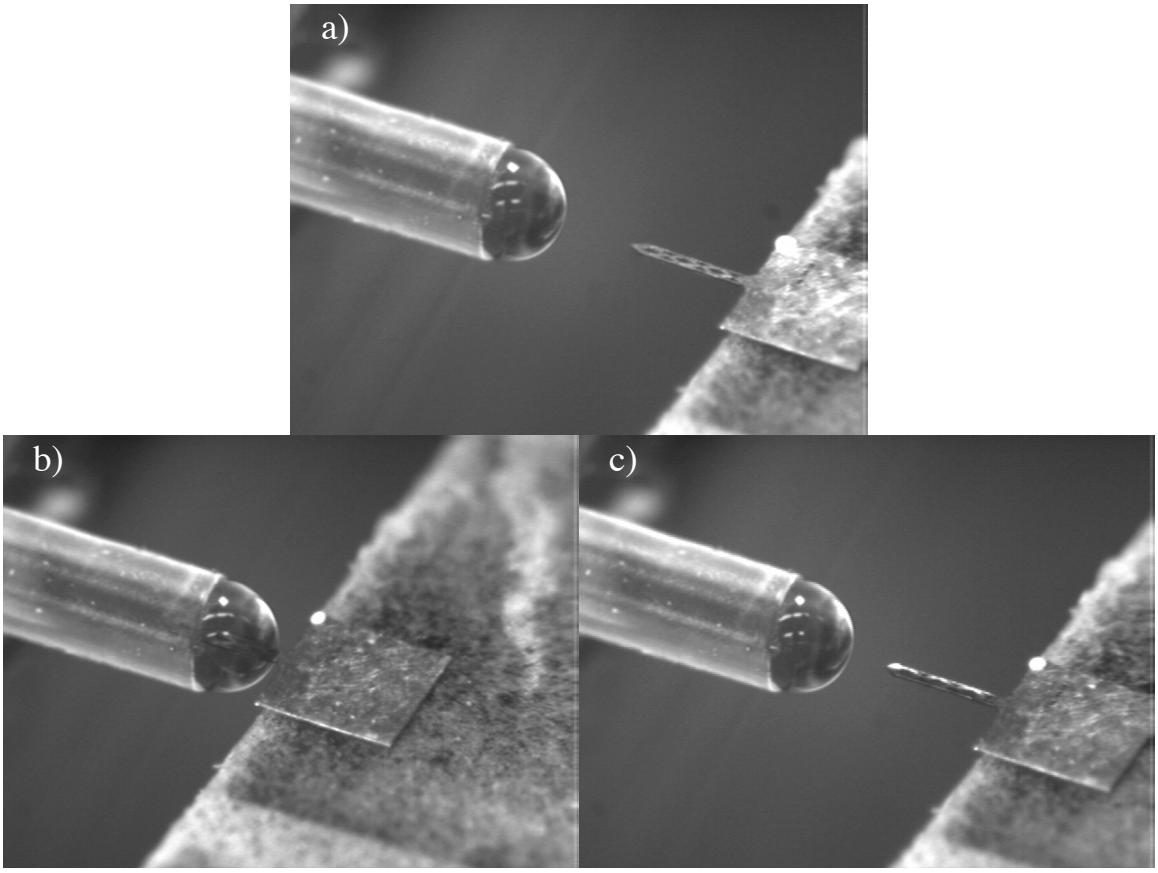

Figure 3-18. Digital photographs of the custom-built MN coating apparatus and coating process for a MN with dimensions of 200 μm width, 50 μm thickness, and 1500 μm length: a) Dispensing formulation; b) Coating the MN; c) Withdrawing the MN.

Fenestrated MNs were examined using fluorescence microscopy to determine the effects the number of dip coats had on coating thickness and fenestration filling. Although this method of visualization did not provide a means for measuring fillings within each fenestration, changes in the fluorescence intensity served as a guide to better understand these effects, i.e., greater fluorescence intensity within a fenestration suggested increased filling volume. As expected, increasing the number of dip coats increased coating thickness and improved fenestration filling uniformity. Results found that single coats provided filling within all fenestrations, however, two to three coats resulted in improved fenestration filling as determined by greater fluorescence intensity within the features. Dip coating greater than three times began to produce excessive coatings on the shank, resulting in non-uniformity along the shank. As it was determined, an optimal number of 3 dip coats was selected for both fenestrated and solid MNs.

Individual fenestrated MNs were coated at a withdraw speed of 1.5 mm/s a total of 3 times each using 3 min intervals between each coat to allow for adequate drying. Individual solid MNs were coating under similar conditions using a withdraw speed of 0.15 mm/s.

Figure 3-19 shows representative fluorescence micrographs of coated solid and fenestrated MNs with identical shank dimensions (200 μm width, 50 μm thickness, and 1500 μm length). Uniform coating is evident in both cases, and deposition of continuous coatings within the fenestrations is observed. Similarly uniform coating and fenestration filling was observed for the other MN design variants as well. Since the coating formulation used for the current study utilizes a common aqueous excipient (i.e., PVP)

and model small molecule drug (i.e., Rhodamine B), this suggests potential for fenestrated MN compatibility with other small molecule drugs that can be formulated under similar conditions.

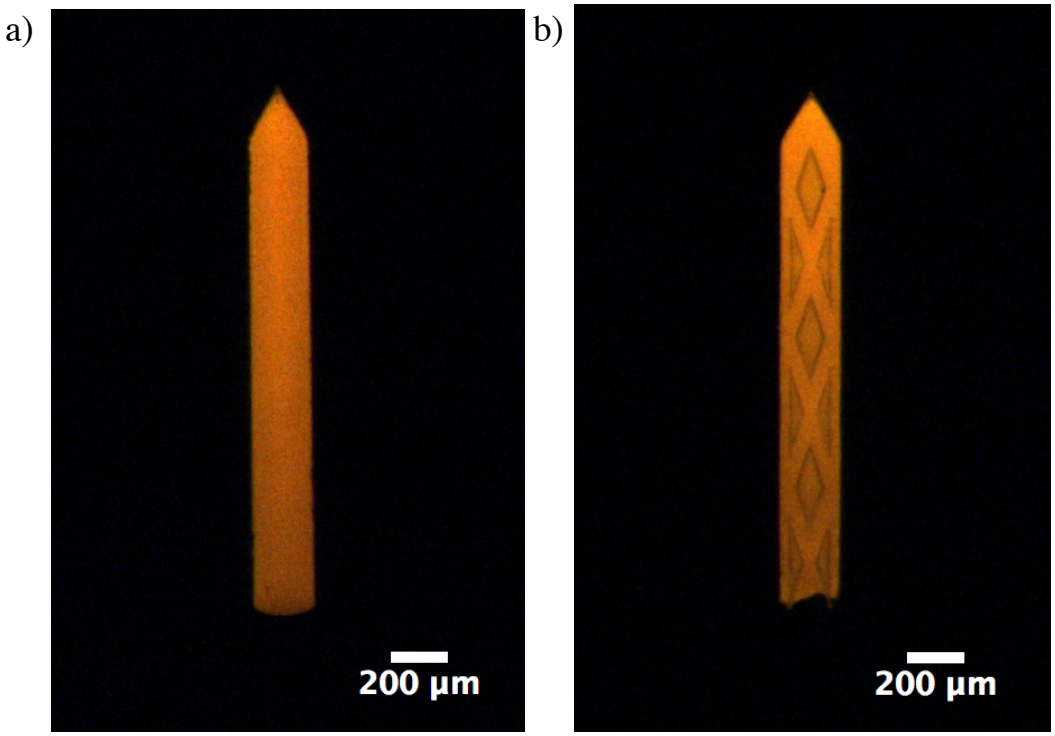

Figure 3-19. Fluorescence micrographs of PVP/Rhodamine B coated solid and fenestrated Ti MNs with identical shank dimensions (200 µm width, 50 µm thickness, and 1500 µm length): a) Coated solid MN; b) Coated fenestrated MN.

Figure F-3 shows a plot of the Rhodamine B intensity calibration curve for the stock coating formulation, generated from a series of dilution measurements. A best fit line with R^2 value of 0.9931 was matched to the data, providing an accurate means for

quantifying coatings. Rhodamine B mass was then calculated based on molecular weight and the known concentration of the initial stock solution.

Figure 3-20 shows a representative plot of the drug mass loadings for solid and fenestrated MNs of identical shank dimensions (1500 μm length, 50 μm thickness, and widths varying from 50 - 200 μm). For all MN lengths shown, the measured mass loadings for fenestrated MNs far exceed those of the comparable solid MNs. Table 3-2 demonstrates that the measured percent increases in mass loading are in good agreement with predicted values for nearly all design variants studied. Table 3-2 further shows that the fenestrated MNs provide up to a five-fold increase in drug carrying capacity relative to solid MNs of comparable size, also in good agreement with predictions.

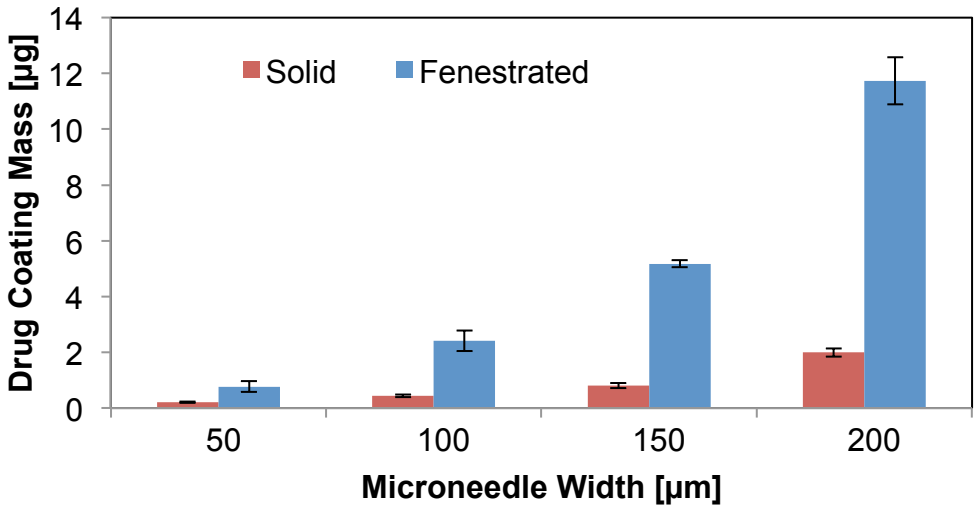

Figure 3-20. Measured drug mass loadings for solid and fenestrated Ti MNs with 1500 μm length, 50 μm thickness, and varying widths. Experimental data points represent average of 6 or more specimens.

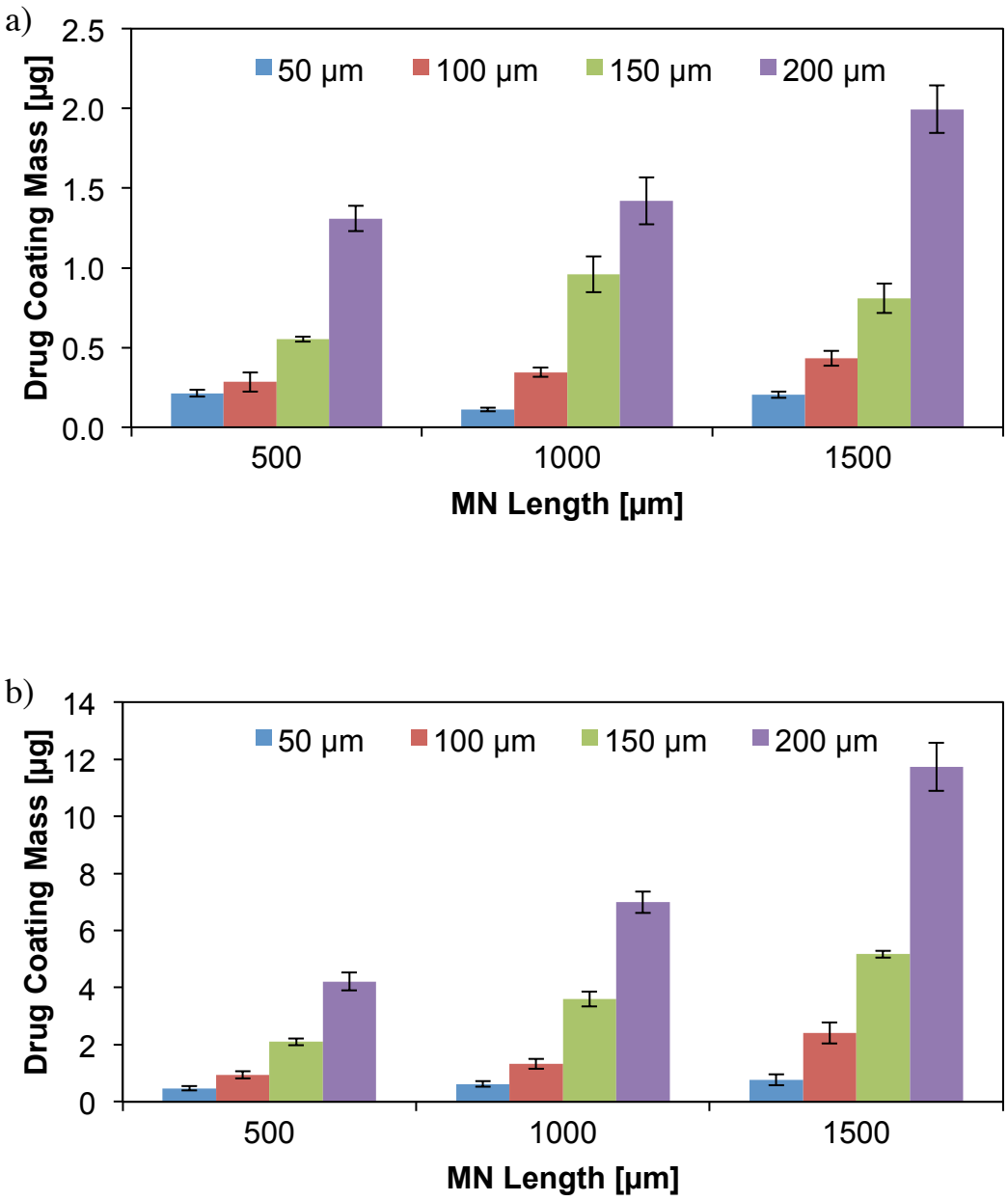

Figure 3-21. Measured drug mass loadings for all Ti MNs design variants with 50 µm thickness, and varying widths and lengths: a) Solid MNs; b) Fenestrated MNs. Experimental data points represent average of 6 or more specimens.

Table 3-2. Estimated and measured increase in drug carrying capacity for fenestrated Ti MNs relative to solid MNs of identical shank dimensions. Measured values are highlighted.

		MN width [μm]							
		50		100		150		200	
MN length [μm]	500	184%	**121%**	210%	**231%**	332%	**280%**	412%	**222%**
	1000	221%	**459%**	247%	**286%**	329%	**275%**	518%	**392%**
	1500	238%	**279%**	293%	**456%**	374%	**539%**	526%	**488%**

As discussed earlier, the increased carrying capacity afforded by the fenestrations may enhance the clinical feasibility of MNs by reducing the array size required for delivery of relevant dosages. As an example, consider the delivery of Pilocarpine, a small molecule drug (M_w = 243 Da) commonly used for the treatment of glaucoma. The conventional dosage requirement for this drug is up to 7500 μg over the course of a 30 day treatment when applied topically via eye drops. However, an analysis by others suggested that MN-based delivery would require only 150 μg, due to the higher bioavailability afforded by MNs (Ninghao 2006). Referring to Figure 3-21a, it can be seen that an array of 75 solid MNs (with 200 μm width, 50 μm thickness, and 1500 μm length) would be required to deliver such a dose. However, in order to also achieve sustained release over the desired treatment duration, formulation of the drug within a nano- or microparticle-based carrier would be required. As such, assuming 10% encapsulation efficiency in such formulations, this would increase the number of solid MNs required by ten-fold to 750. Assuming a needle pitch of at least 5 times the needle width and thickness (to ensure reliable needle insertion and minimized tissue

deformation), this would require an array size of at least 27 mm x 27 mm, which is prohibitively large for use on human eyes. However, referring again to Figure 3-21b, it can be seen that comparable fenestrated MNs could carry up to five times more drug per needle, thus allowing reduction of the array size to 11 mm x 11 mm, which is well within the range of feasibility.

While the demonstration of fenestrated MN arrays is beyond the scope of the current study, their fabrication is expected to be fully compatible with the Ti DRIE process. For example, linear arrays of in-plane MNs could be fabricated using the same process described herein, followed by their stacking and bonding to form three-dimensional arrays, as has been demonstrated for high-density microelectrode arrays for neural prosthetic interfaces (Hoogerwerf and Wise 1994; Bai, Wise, and Anderson 2000). Alternatively, planar arrays of in-plane MNs could be fabricated, followed by their plastic deformation out-of-plane, as has been demonstrated for transdermal and other drug delivery applications (Gill and Prausnitz 2007b; Gill and Prausnitz 2007a). The latter approach is likely to be more amenable to low-cost/high-volume manufacturing, thus making it the more attractive, since disposability may be ultimately required for clinical and commercial feasibility, as discussed earlier.

3.4.4. Drug Delivery

Figure 3-22 shows representative histological sections and fluorescence overlay micrographs of excised rabbit corneas at the insertion sites of coated solid and fenestrated MNs with 200 μm width, 50 μm thickness, and 500 μm length. The images confirm MN penetration into the cornea to a depth of ~300 μm, which is roughly half that of the MN

length. This is consistent with observations by others, and is due to tissue deformation prior to penetration (J Jiang et al. 2007). These results demonstrate the capability provided by MNs for precisely penetrating into, but not through the cornea, thus enhancing safety relative to intravitreal injection. Moreover, the ability to achieve MN insertion manually (i.e., non-surgically) demonstrates the inherent simplicity of this approach.

Figure 3-21 also demonstrates that intracorneal drug delivery can be achieved with Ti MNs, as evidenced by the Rhodamine deposition within the tissue at the insertion site. Moreover, the images show that fenestrated MNs can enhance drug deposition beneath the tissue surface relative to solid MNs, as evidenced by the greater ratio of sub-surface to sub-surface Rhodamine intensity at the fenestrated MN insertion site. This is due to the protection afforded by the fenestrations, which reduces potential for shear-induced coating loss at the tissue surface during MN insertion. This is a key point, since it suggests potential for more efficient and reliable delivery of the desired dosage *in vivo*.

a)

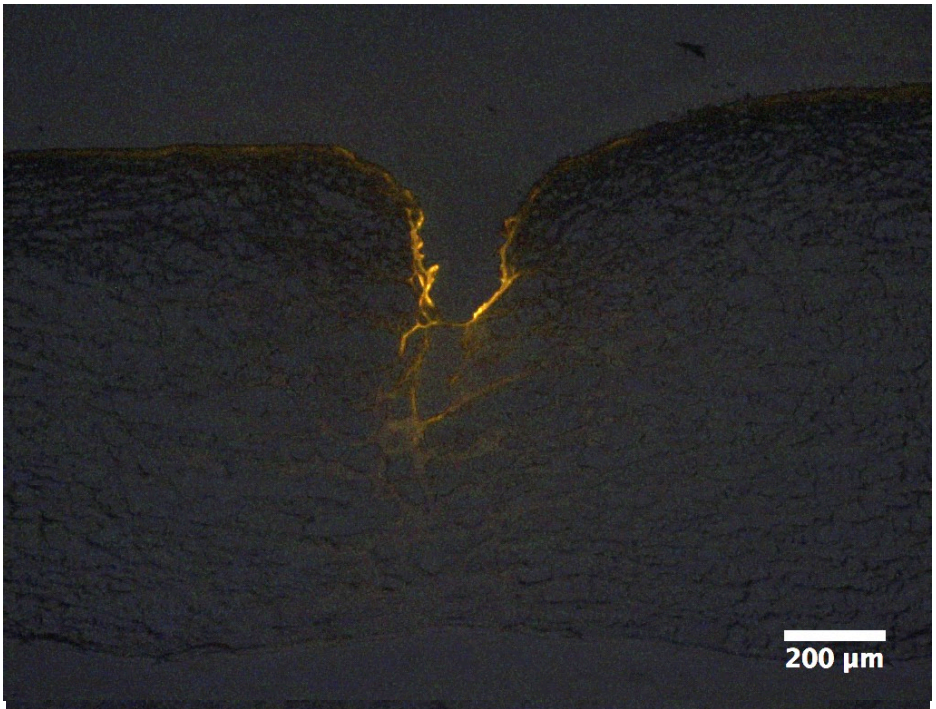

b)

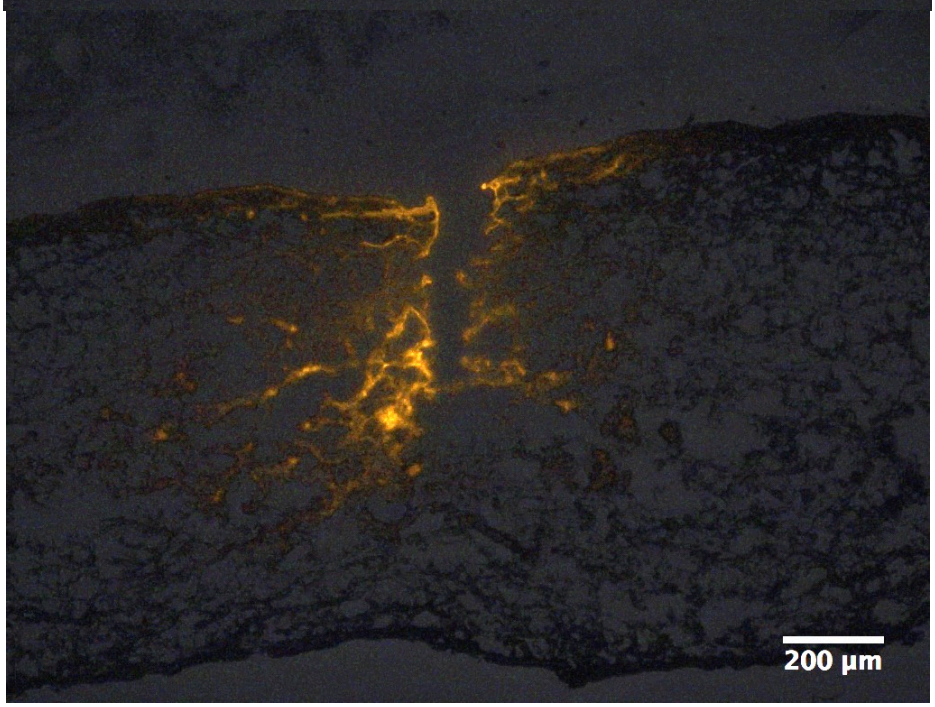

Figure 3-22. Histological sections and fluorescence overlay micrographs of excised rabbit corneas at the penetration sites of coated solid and fenestrated Ti MNs with 200 µm width, 50 µm thickness, and 500 µm length: a) Solid MN; b) Fenestrated MN.

3.5. Conclusions

We have reported the design, fabrication, and characterization of fenestrated Ti MNs for ocular drug delivery. We have demonstrated that these devices possess sufficient stiffness for reliable corneal insertion, and also provide potential for enhanced safety, due to their graceful, plasticity-based failure mode. Moreover, uniform deposition of a fast-dissolving model drug coating formulation has been demonstrated, as has significant enhancement of drug carrying capacity relative to comparable solid MNs. Finally, results from insertion studies in excised porcine cornea corroborate many of these findings by demonstrating capability for reliable MN insertion and drug delivery. Collectively, these results begin to demonstrate the potential embodied in fenestrated Ti MNs for providing safe, simple, and efficacious means for ocular drug delivery. They also motivate the exploration of the potential for use of fenestrated MNs with nano- or microparticle-entrained MN coatings, since this may provide opportunity for achieving sustained delivery, and thus, reduced treatment frequency.

4 TITANIUM ANODIC BONDING FOR MICROFLUIDIC APPLICATIONS

4.1. Introduction

As discussed in previous sections of this dissertation, the recent advent of techniques for deep reactive ion etching of titanium (i.e., Ti DRIE) provides new opportunities for exploiting the advantageous properties of Ti for the realization of microfluidic devices with enhanced robustness, performance, and functionality. However, the intrinsic opacity of Ti precludes optical interrogation within many Ti-based microfluidic devices, thus limiting potential for extension to emerging areas such as optofluidics-based medical diagnostics, water treatment, and hydrocarbon fuel production (Erickson, Sinton, and Psaltis 2011; Chen et al. 2012). This, therefore, motivates the development of methods for bonding transparent substrates to Ti.

Interlayers or adhesives provide a means for addressing this need. However, this often adds significant process complexity, particularly when selective placement of these materials with micro-scale precision is required. Moreover, thermal stability, chemical compatibility, and hermeticity considerations may further limit the scope of applications where interlayers or adhesives may be used. Finally, similar limitations are inherent to many of the common polymeric materials that could be considered for use as transparent substrates. Consequently, this motivates the development of techniques that allow interlayer- and adhesive- free bonding of Ti to glass-based substrates, since glass provides greater rigidity, chemical resistance, and thermal stability than typical polymers.

4.1.1. Anodic Bonding

Anodic bonding, also known as field assisted bonded or electrostatic sealing, which is widely used for sealing of conventional silicon or metal-based substrates to glass, represents a promising option in regards to applications for microfluidics and microelectromechanical systems (K. M. Knowles and A. T. J. van Helvoort 2006). This is due, in large part, to the potential opportunity it affords for high-strength, hermetic bonding at relatively low temperatures ($T \leq 400°C$). However, thus far, there has been only limited study of anodic bonding of metallic substrates. Moreover, of these studies, even fewer have explored the anodic bonding of Ti specifically (George Wallis 1969; Toyoda et al. 1993; Briand, Weber, and F. de Rooij 2004; Shu et al. 2008). Finally, of these few studies, none have reported successful wafer-scale anodic bonding of bulk Ti and glass substrates. Since the development of wafer-scale bonding is critically important for ensuring the potential for scalable manufacturing of Ti/glass-based microfluidic devices, this motivates the development of techniques that can provide such capability.

4.1.2. Scope of this Work

Herein, we demonstrate the first anodic bonding process that provides the capability for wafer-scale anodic bonding of bulk Ti and glass substrates. We show that uniform, full-wafer bonding can be achieved at temperatures well below those of previously reported Ti anodic bonding studies, which opens potential for greater process versatility and material compatibility. Furthermore, using burst pressure testing, we show that the bond strengths exceed the strength of the glass, which demonstrates the

robustness of the bonding. When used in conjunction with our Ti DRIE capability, we also show that the anodic bonding process enables fabrication of Ti/glass-based microfluidic devices at the wafer-scale. Finally, we show that nanoporous titanium dioxide can be easily integrated within such devices via in situ growth directly from the Ti channel surfaces, which therefore opens new opportunity for realization of robust microfluidic devices for photocatalysis applications.

4.2. Materials and Methods

4.2.1. Anodic Bonding Mechanism

As illustrated in Figure 4-1, anodic bonding relies on the use of substrate heating and applied voltage to drive mobile cations (Na^+) in the glass substrate towards the cathode. This results in creation of a negatively charged depletion layer in the glass adjacent to the anode substrate, which produces an electric field within the layer. When coupled with the electric field that also arises within the air gap between the substrates, large electrostatic forces are produced that bring the substrates into intimate contact. Permanent bonds are then formed via anodic oxidation at the interface between the substrates. Although this mechanistic understanding has been developed primarily within the context of silicon anode substrates, it has been shown to be applicable to a number of metals as well (e.g., Kovar, Al, and Fe) (K. M. Knowles and A. T. J. van Helvoort 2006).

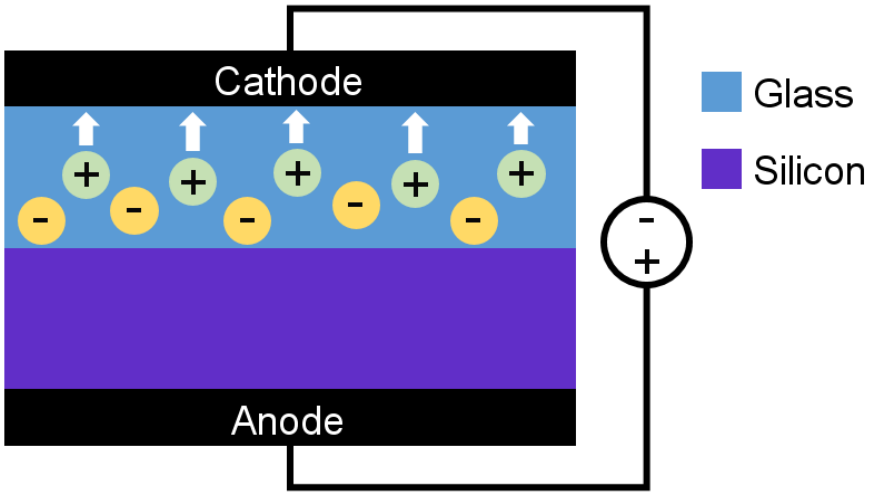

Figure 4-1. Schematic of the anodic bonding mechanism for silicon and glass substrates (and a number of metal/glass systems as well).

4.2.2. Bond Process Parameters

Commercial substrate bonders allow for unique process control and development through by varying the following parameters: applied tool force, chamber pressure, applied voltage, substrate temperature, and process time. Parameter values can depend greatly on the material properties, geometry, and substrate surface finish. As a result, a thorough study of process parameters was required to achieve optimal bonding conditions for our titanium substrates, specifically.

Determining the force to apply requires that loads not induce too much residual stress in the stack to cause premature cracking of the glass substrate, while maintaining enough of a force to allow for good contact between the surfaces. Typical processes apply a small, uniform compressive stress (< 0.5E5 mbar) to the substrate stack to ensure

good contact is made between the surfaces in preparation for sealing via anodic oxidation.

Successful anodic bonding at atmospheric pressure has been demonstrated, and provides the added benefit of simplicity by utilizing a standard laboratory hotplate and voltage source setup. However, bonding under vacuum serves the benefit of reducing the potential for air pockets to become entrapped between the substrates prior to sealing, which can cause incomplete bonding over the area of the substrates. Furthermore, isolating the specimens in a vacuum chamber may reduce the risk for particle contamination that may arise otherwise. As a result, typical bonding processes utilize chamber pressures less than 1E−3 mbar.

Anodic bonding commonly uses a plate anode electrode to uniformly apply voltages between 100 and 1500 V over the stack of the two materials to be bonded. However, point electrodes have also been utilized to initiate bonding. Point electrodes differ from plate electrodes in that when voltage is applied, intimate contact between the substrates grows radially outward from the original point of contact, and thus homogeneous bonding does not occur across the area of the substrates simultaneously. Plate electrode systems provide a more homogeneous electric field distribution, and therefore is the preferred technique for the scope of this work.

Temperature is considered one of the most important parameters during the bond process. Elevating temperatures increases the potential for enhanced ion mobility in the glass substrate due to greater kinetics, thereby producing a greater depletion zone at the bond interface and increasing the potential for strong oxidative bonds to form at the

interface of the substrates. However, coefficient of thermal expansion (CTE) mismatching of materials puts limits on allowable processing temperatures. Although care can be taken to select a glass substrate with similar CTE to Ti, increased heating can ultimately lead to excessive residual stress buildup in the substrates upon cooling to room temperature, causing premature cracking of the glass.

Lower bond temperatures are generally favorable to ensure good process integration with existing device specific fabrication flows (e.g., metallization or sputtering) which may be sensitive to excessive heating. In general, processing temperatures of 200 to 400°C have been shown to be effective for anodic bonding of various metal and glass substrates (K. M. Knowles and A. T. J. van Helvoort 2006).

4.2.3. Substrates

To ensure quality bonding, substrates must be flat, smooth, and clean. The process of anodic bonding is preferred over other sealing techniques due to its tolerance for greater substrate surface roughness, where root mean square value (RMS) surface roughness values between 0.02 to 0.05 μm generally being acceptable (van Helvoort et al. 2004; George Wallis, Dorsey, and Beckett 1971). Foreign contaminant particles caught between the substrates to be bonded may inhibit full-scale hermetic sealing, and as a result, stringent substrate cleaning procedures must be followed to ensure quality bonding. For this reason, processing substrates in a cleanroom facility with micron-scale particle filtering is preferred, and improves the potential to produce high-quality, reproducible results.

Table 4-1 lists relevant properties of the wafer-based Ti and glass substrates used in the current study (Tokyo Stainless Grinding Co., and Mark Optics, Santa Ana, CA respectively). The Ti wafers were composed of polycrystalline, CP Grade 1 Ti, and they were manufactured by punching from large polished sheets, which resulted in subtle edge burr induced non-planarity at the wafer perimeter. The glass wafers were composed of N-BK7, a borosilicate crown glass commonly used for high-quality optical components, due to its optical quality, purity, and excellent transmittance from 350 to 2000 nm. Although the use of N-BK7 for anodic bonding has yet to be reported, its selection for the current study was motivated by: (a) its closely matched CTE, which is crucial for moderating residual stresses produced by differential contraction of the Ti and glass substrates during cooling from bonding; and (b) its superior optical quality relative to other glasses with similar CTEs (e.g., D263, soda lime glass, Foturan, etc.).

Table 4-1. Titanium and N-BK7 glass wafer properties.

Substrate	α (1E-6°C^{-1}) 20-300°C	E (GPa)	ν	Wafer diameter (mm)	Wafer thickness (μm)	RMS surface roughness (nm)
Titanium	9.3	108	0.35	100	500	0.6
N-BK7	8.3	82	0.206	100	500	2.0

4.2.4. Bonding

Prior to bonding, the wafers were cleaned by sequential ultra- sonic agitation in acetone and isopropanol, followed by deionized (DI) water rinsing and N_2 drying. The wafers were then loaded into a commercial wafer bonder (SB6-E, Suss Microtec, Germany) and bonded under the following process conditions: temperatures ranging from 200 to 400°C; 300 V applied voltage; 5E−3 mbar chamber pressure, 225 mbar tool force, and 3 min bond time.

4.2.5. Residual Stress Estimation

The residual stresses in the glass were estimated using the following expression (Ohring 1992):

$$\sigma_{\mathrm{g}} = \frac{1}{t_{\mathrm{g}}} \cdot \frac{\left(\alpha_{\mathrm{m}} - \alpha_{\mathrm{g}}\right) \Delta T}{\frac{1 - v_{\mathrm{g}}}{t_{\mathrm{g}} E_{\mathrm{g}}} + \frac{1 - v_{\mathrm{m}}}{t_{\mathrm{m}} E_{\mathrm{m}}}}$$

where t_g and t_m are the thicknesses of the glass and metal wafers, α_g and α_m are the CTEs, v_g and v_m are the Poisson's ratios, and E_g and E_m are the elastic moduli. For the bonding temperatures used in the current study, this predicted compressive residual stresses in the glass ranging from 13.8 to 29.0 MPa.

4.2.6. Bond Integrity Characterization

Characterization of bond integrity was performed using hydraulic burst pressure testing, since this provided a more application-specific evaluation method than commonly used tensile testing. As shown in Figure 4-2, test specimen preparation began

with the photolithographic patterning of a 2 × 2 array of fluidic reservoirs (6.35 mm diameter) uniformly spaced across the Ti wafers (SU-8 2075, MicroChem). The mask pattern was then projected into the substrates to a depth of 100 μm using the Ti DRIE process (E640-ICP, Panasonic Factory Solutions; Process conditions: 15 mT chamber pressure, 400 W ICP source power, 200 W substrate power, 100 sccm Cl_2 , and 5 sccm Ar). Through-wafer vias (1.59 mm diameter) were then defined within the etched reservoirs using a manually operated mill to provide fluidic access to the reservoirs. Finally, the photoresist mask was stripped and anodic bonding was performed to seal the reservoirs. It is important to note that Ti DRIE could also be used to define the through-wafer vias. However, its use for such purposes in the current study was not sufficiently justified, due to the relatively large size and spacing of the vias, as well as their limited numbers.

Figure 4-2. Fabrication process for burst pressure testing specimens: a) Lithographic patterning of Ti, followed by Ti DRIE to define micromachined fluidic reservoirs within the Ti substrate; b) Through-wafer via definition using manual milling to provide fluidic access to the reservoirs; c) Anodic bonding with N-BK7 substrate to seal the reservoirs.

Individual test specimens were diced from the bonded wafers (7100 Series Dicing Saw, Advanced Dicing Technologies, Yokneam, Israel), and stainless steel liquid chromatography (LC) tubing was attached to the backside of the Ti substrates using epoxy. After air purging, DI water was pumped into the test specimens at 0.1 μl/min using a high-pressure syringe pump with integrated pressure transducer (100DM, Teledyne ISCO, Lincoln, NE). Pressure data were recorded, and each test was halted after the sharp pressure drop that accompanied specimen failure. Burst pressure was defined as the maximum pressure achieved during testing.

4.3. Results and Discussion

4.3.1. Bonding

Figure 4-3 shows a digital photograph of Ti and N-BK7 wafers successfully anodically bonded at 300°C. Similar results were obtained for wafers bonded at temperatures ranging from 250 to 375 °C. Uniform bonding across the entirety of the wafers is evident, with the exception of a thin annulus of glass lost at the perimeter, due to the edge burr of the underlying Ti wafer. The brown coloration in the image is the interfacial oxide reaction product, which has been observed in anodic bonding of other metals (e.g., Kovar/Pyrex) (G. Wallis 1970). Reliable full-wafer bonding was not observed at bonding temperatures below 250°C, presumably due to insufficient cation mobility, and partial delamination and cracking of the glass substrate often occurred at bonding temperatures above 375°C, due to excessive residual stress.

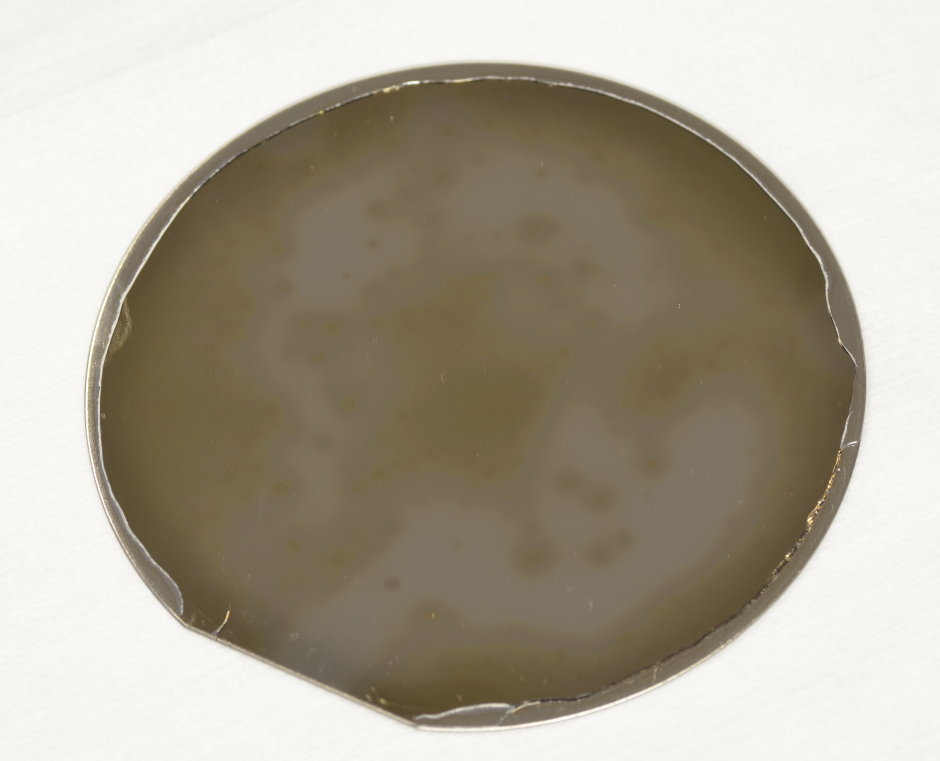

Figure 4-3. Digital photograph of 100 mm diameter, 500 μm thick Ti, and N-BK7 glass wafers anodically bonded at 300°C.

The achievement of uniform, full-wafer bonding herein stands in contrast to earlier Ti anodic bonding studies, which were unable to achieve reproducible bonding at the chip-scale (Toyoda et al. 1993; Briand, Weber, and F. de Rooij 2004), only demonstrated partial bonding at the wafer-scale (Shu et al. 2008), or provided no evidence supporting claims of successful bonding (George Wallis 1969). Moreover, the achievement of bonding at significantly lower temperatures than those used in earlier studies (i.e., 250°C herein vs. 400°C or higher in (Briand, Weber, and F. de Rooij 2004; Shu et al. 2008)) suggests potential for greater process versatility and material

compatibility, since residual stresses and thermal budget are reduced. This will be particularly important for future applications requiring anodic bonding of Ti-based device substrates with previously deposited thin-film dielectrics and metallizations (e.g., for applications requiring both optical and electrical interrogation).

4.3.2. Burst Pressure Testing

Figure 4-4 shows close-up digital photographs of anodically bonded specimens fabricated for burst pressure testing. As seen in Figure 4-4a, uniform bonding was achieved over the reservoirs in the underlying Ti, thus demonstrating that the anodic bonding process is compatible with substrates micromachined by Ti DRIE. Moreover, as shown in Figure 4-4b failure during burst pressure testing was typically observed to occur via cracking of the glass at the periphery of the reservoir, rather than delamination at the Ti/glass interface.

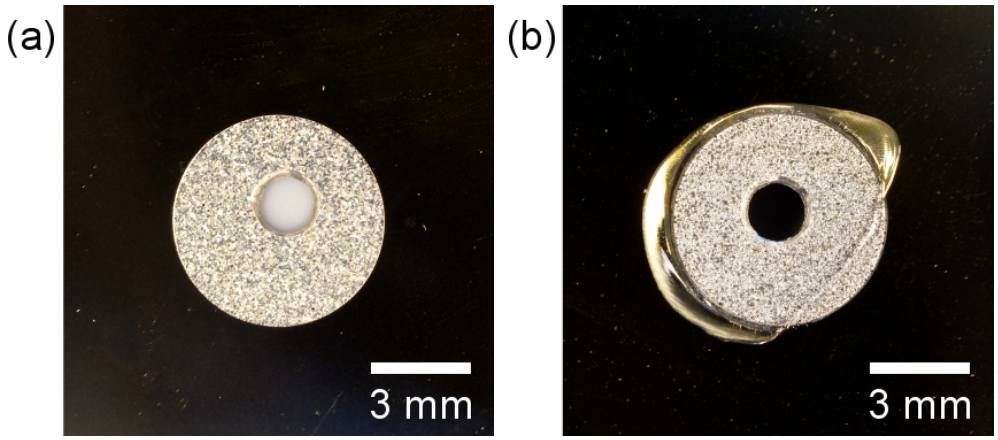

Figure 4-4. Digital photographs of anodically bonded BPT specimens at the reservoir region: a) Specimen prior to testing; b) Ruptured specimen after testing.

Figure 4-5 shows a plot of the measured burst pressure as a function of specimen bonding temperature. The data shows that burst pressure was largely consistent across all bonding temperatures tested, with a mean value of 1.02 ± 0.12 MPa. The achievement of comparable strength bonding at lower bond temperatures (e.g., 250°C versus 375°C) is favorable, as it implies the potential to integrate Ti anodic bonding with existing device specific fabrication flows that require lower processing temperatures.

Many anodic bonding studies report strong dependence of bond strength on bonding temperature. However, the absence of such dependence in the current study, coupled with the observation of cracking at the reservoir periphery, demonstrates that the

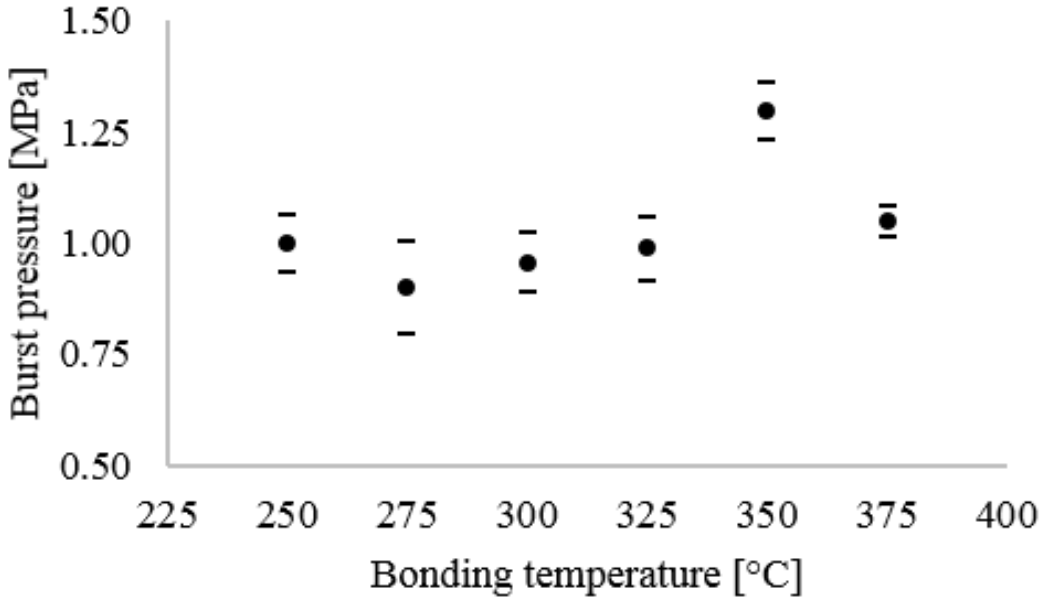

Figure 4-5. Plot of the measured burst pressure as a function of specimen bonding temperature. Data = mean ± standard deviation, n ≥ 3.

strength of the Ti/glass interface was not probed, but rather the strength of the glass itself. For a rigidly clamped, circular diaphragm subjected to uniform applied pressure P, the maximum radial stress occurs at the periphery and is given by (Di Giovanni 1982):

$$(\sigma_{\mathrm{r}})_{\max} = \pm\frac{3}{4}\frac{Pa^2}{h^2}(1-v)$$

where a and h are the radius and thickness of the diaphragm, respectively, and ν is the Poisson's ratio of the diaphragm material. For the current study, this yields maximum radial stress of 37.2 MPa in the glass at the measured mean burst pressure. This is in good agreement with the reported failure strength of N-BK7, which ranges from 50.3 to 70.6 MPa, depending on the surface condition (Shott North America 2004). This, therefore, suggests that higher pressures could be tolerated with reduction of the reservoir diameter and/or increase of the glass substrate thickness. However, it is clear that maximum pressure tolerance will ultimately be dictated by the bond strength of the Ti/glass interface.

4.3.3. Device Fabrication Demonstration

To demonstrate the functionality of Ti anodic bonding, rudimentary microfluidic devices were fabricated using a process similar to that of the burst pressure test specimens. As before, Ti and N-BK7 glass wafers were used, each with 100 mm diameter and 500 μm thickness. An optimum bonding temperature of 300°C was selected to ensure sufficiently high bond strength, while minimizing risk for residual stress-induced

delamination. The devices employed a serpentine channel design produced by Ti DRIE, with a channel width of 100 μm, a channel depth of 21 μm, and channel pitches varying from 200 to 600 μm. Figure 4-6 shows a digital photograph of a completed device wafer after anodic bonding, which demonstrates that uniform, full-wafer bonding was achieved over the device structures.

To demonstrate the capabilities of Ti anodic bonding for microfluidic applications, select fluidic devices on the wafer were tested. Using LC tubing and fixtures, a syringe filled with an ethanol/dye solution (Rhodamine B, Sigma) was connected to microfluidic devices of varying pitch. Figure 4-7 shows a digital photograph of the device operating at the wafer scale. Figure 4-8 shows close-up digital photographs of microfluidic devices with varying pitch operating under leak-free pressure driven flow. These results demonstrate the capability for using Ti anodic bonding in combination with Ti DRIE to fabricate and operate microfluidic devices at the wafer scale. These results are in stark contrast to previous studies of Ti anodic bonding, which were unable to achieve such results.

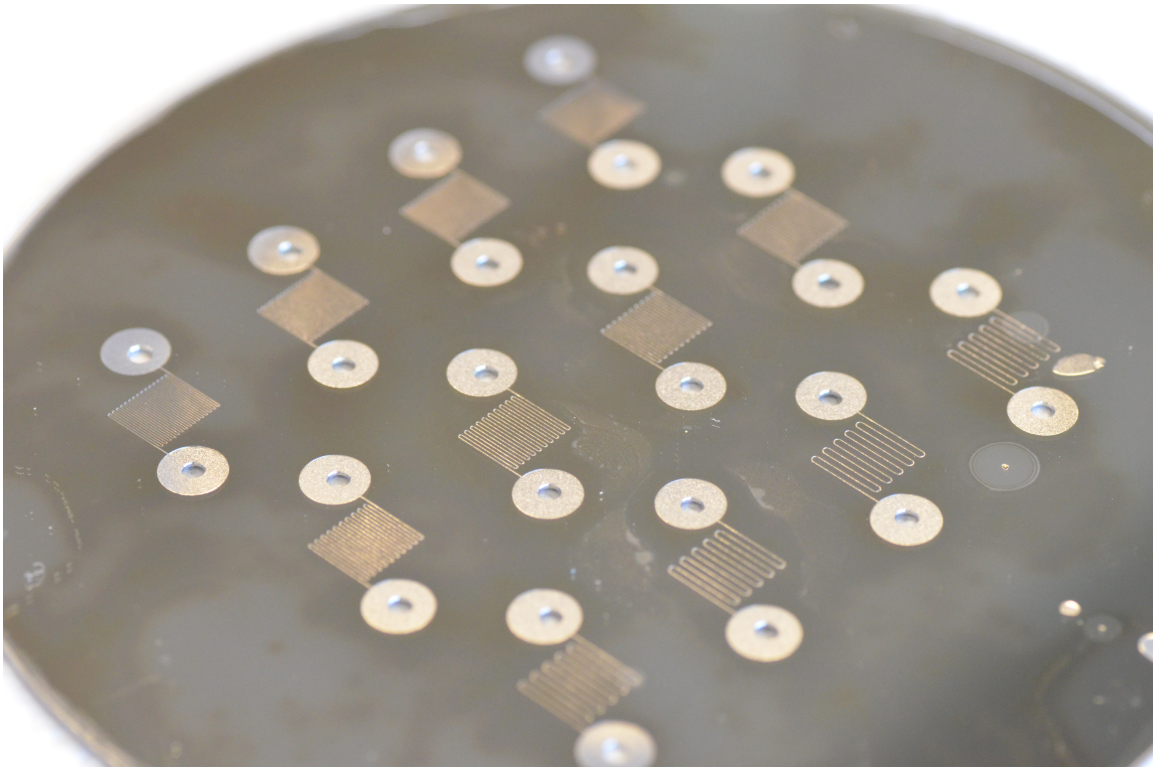

Figure 4-6. Digital photograph of full wafer-scale anodically bonded Ti microfluidic device showing array of devices with 100 μm channel width and channel pitches ranging from 200 to 600 μm.

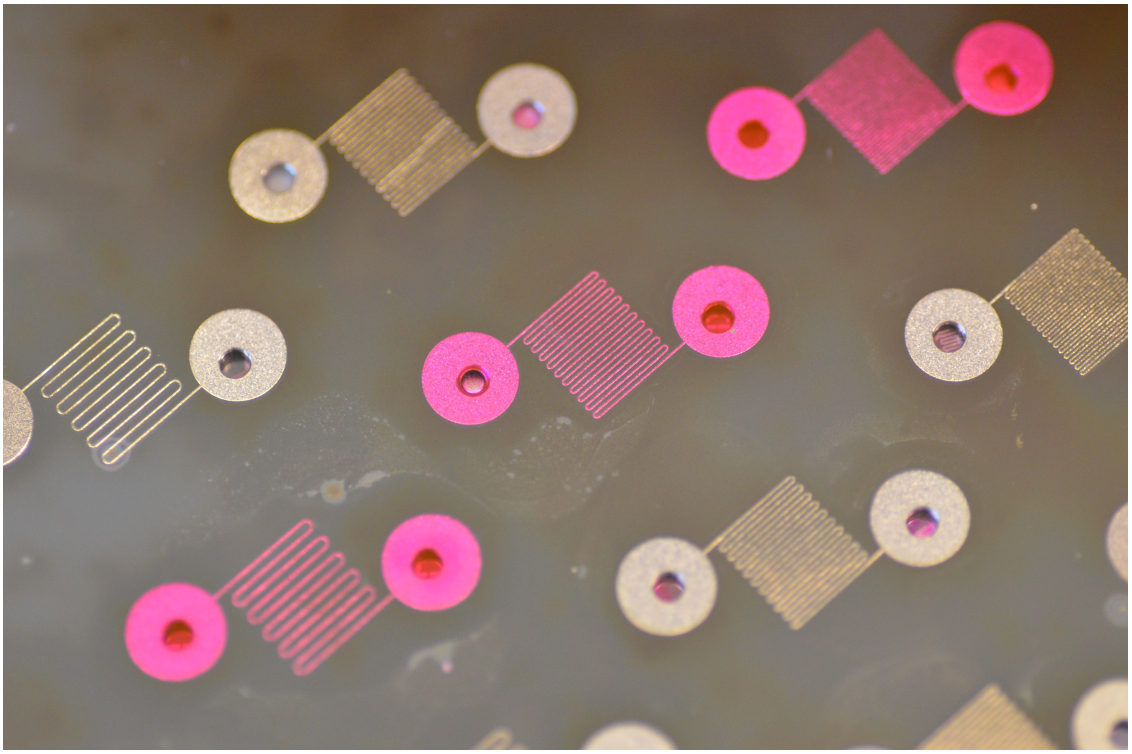

Figure 4-7. Digital photograph of wafer scale anodically bonded Ti microfluidic devices with 100 μm channel width and channel pitches ranging from 200 to 600 μm under simultaneous pressure-driven flow of ethanol/dye solution.

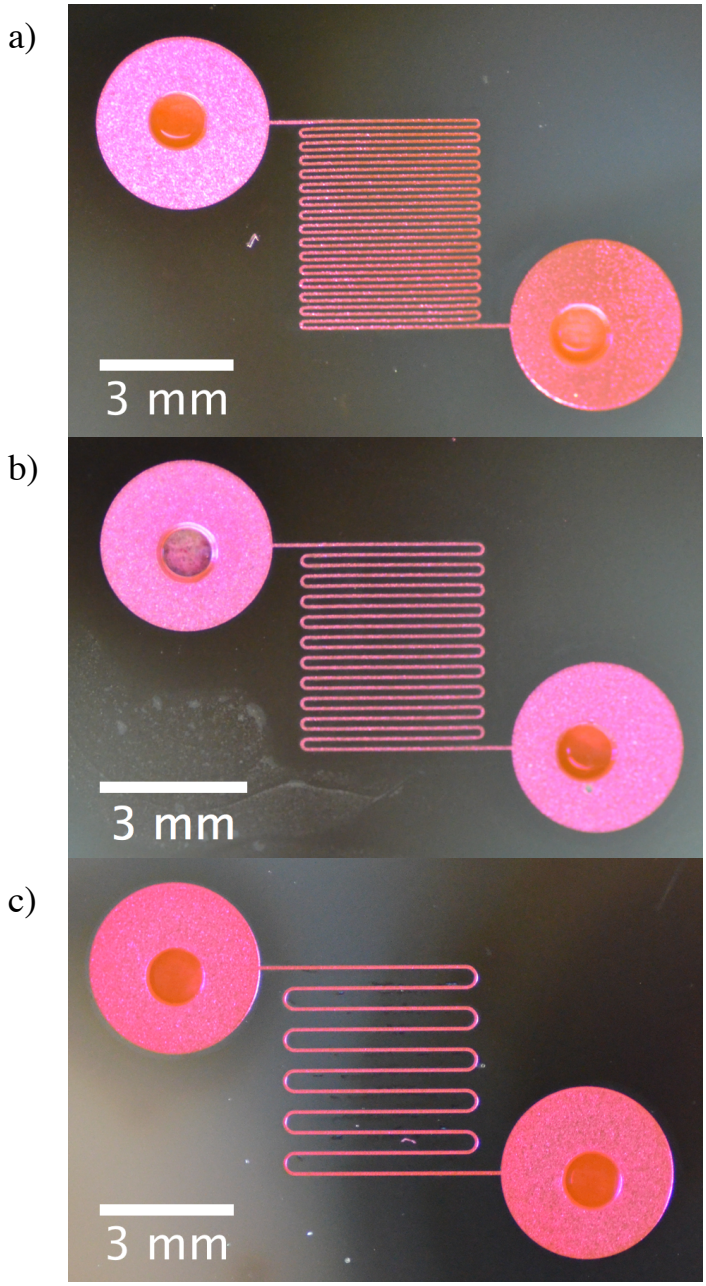

Figure 4-8. Digital photographs of pressure driven flow of ethanol/dye solution within bonded devices of 100 µm channel width varying pitch: a) 200 µm pitch; b) 300 µm pitch; c) 600 µm pitch.

To further demonstrate the robust capabilities of Ti anodic bonding for microfluidic and lab-on-chip applications, it was necessary to show that wafer scale devices could be diced for chip scale testing. After fabrication, individual devices were diced from the bonded wafers and fluidic interconnects (NanoPorts, Upchurch Scientific) were affixed to the backside of the chips. LC tubing was used to connect the devices to a manual syringe filled with an ethanol/dye solution. Figure 4-9 shows a digital photograph taken during pressure-driven flow though a device with 300 μm channel pitch. The observed confinement of flow to the channels further confirms the high quality of anodic bonding over micromachined features in the underlying Ti substrate. Furthermore, the ability to dice wafers with no visible delaminated or debonded areas at the periphery of the chip suggests the bond strength is sufficiently high and this process can be used to fabricate devices of various sizes and geometries.

The development of Ti anodic bonding, coupled with our existing Ti DRIE capability, opens potential for fabrication of robust analogues of conventional Si- and glass-based microfluidic devices requiring optical interrogation. It also enables the creation of optically accessible devices with greater rigidity, chemical resistance, and thermal stability than polymer-based devices. However, when further combined with the potential for easily integrating nanoporous titanium dioxide (TiO_2) within anodically bonded Ti devices, we believe even greater promise may eventually lie in the opportunity for realization of robust, high-performance devices for photocatalytic microreactor applications.

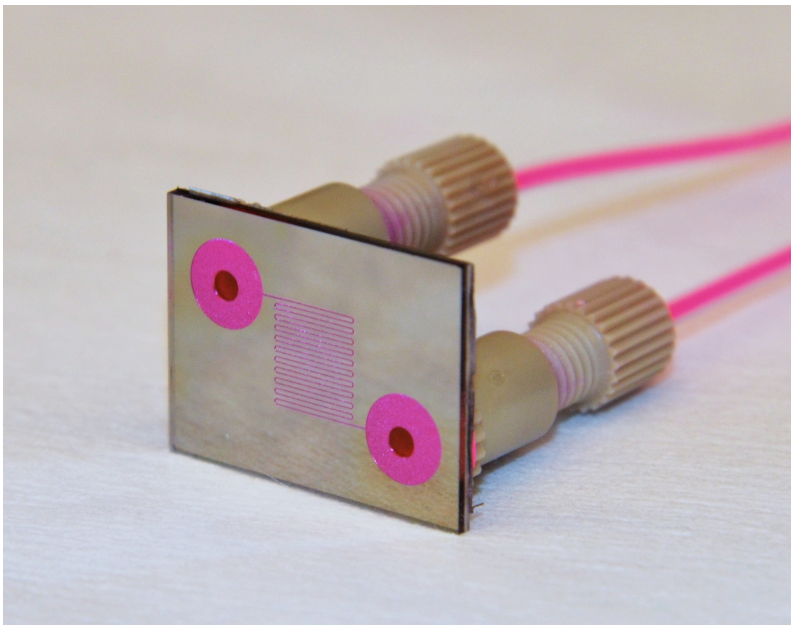

Figure 4-9. Digital photograph of pressure-driven flow of ethanol/dye solution within 300 μm channel pitch anodically bonded Ti microfluidic device at the chip scale.

4.3.4. Monolithic Integration of Nanoporous TiO_2

Titanium dioxide is a well-known photocatalyst (Fujishima, Zhang, and Tryk 2008) and its use in microfluidic devices has received considerable attention since the first demonstration of a TiO_2-based photocatalytic microreactor nearly a decade ago (Gorges, Meyer, and Kreisel 2004). Examples of device applications reported since then include those for water purification (Lei et al. 2010), water splitting (Ahsan, Gumus, and Erickson 2013), and photochemistry (Takei, Kitamori, and Kim 2005; Matsushita et al. 2006), among others. The photocatalytic properties of TiO_2 have also been exploited as a novel means for achieving microfluid control (Takei, Kitamori, and Kim 2005; Nagai et

al. 2007) and site-specific nanoparticle synthesis in situ (Castellana et al. 2006). In many of these applications, miniaturization affords opportunity for significantly enhancing performance relative to conventional bulk reactors, due to increased surface area, reduced diffusion length, and greater uniformity of irradiation. However, low volumetric throughput remains a critical limitation in many applications, as does the difficulty associated with integrating TiO_2 uniformly within complex device geometries (Ning Wang et al. 2013).

Figure 4-10 shows one approach for addressing these limitations via the monolithic integration of nanoporous TiO_2 (NPT) within an anodically bonded, Ti-based microfluidic device. In this approach, NPT is grown in situ, directly from the Ti channel surfaces using an aqueous H_2O_2 oxidation process reported earlier (A. S. Zuruzi and MacDonald 2005). As illustrated in the scanning electron micrograph in Figure 4-10a, in situ growth is advantageous, since it allows for conformal coverage of complex geometries that would be difficult, if not impossible to coat uniformly using conventional sol–gel or thin-film deposition routes. Moreover, as shown in Figure 4-10b, the reticulated, open-framework porosity of the NPT provides higher surface area than dense TiO_2 films, and greater fluidic accessibility to the photocatalyst surfaces relative to nanoparticle-based films, thus suggesting potential for higher reaction rates. Finally, when combined with the intrinsic toughness of Ti, opportunity may be afforded for the fabrication of robust, large-area photocatalytic devices that can provide volumetric throughputs approaching those required for commercial feasibility in many applications. Studies are currently underway to further explore this opportunity. Details regarding NPT

growth conditions, morphology, composition, and structure can be found in (Abu Samah Zuruzi et al. 2013; A. S. Zuruzi and MacDonald 2005).

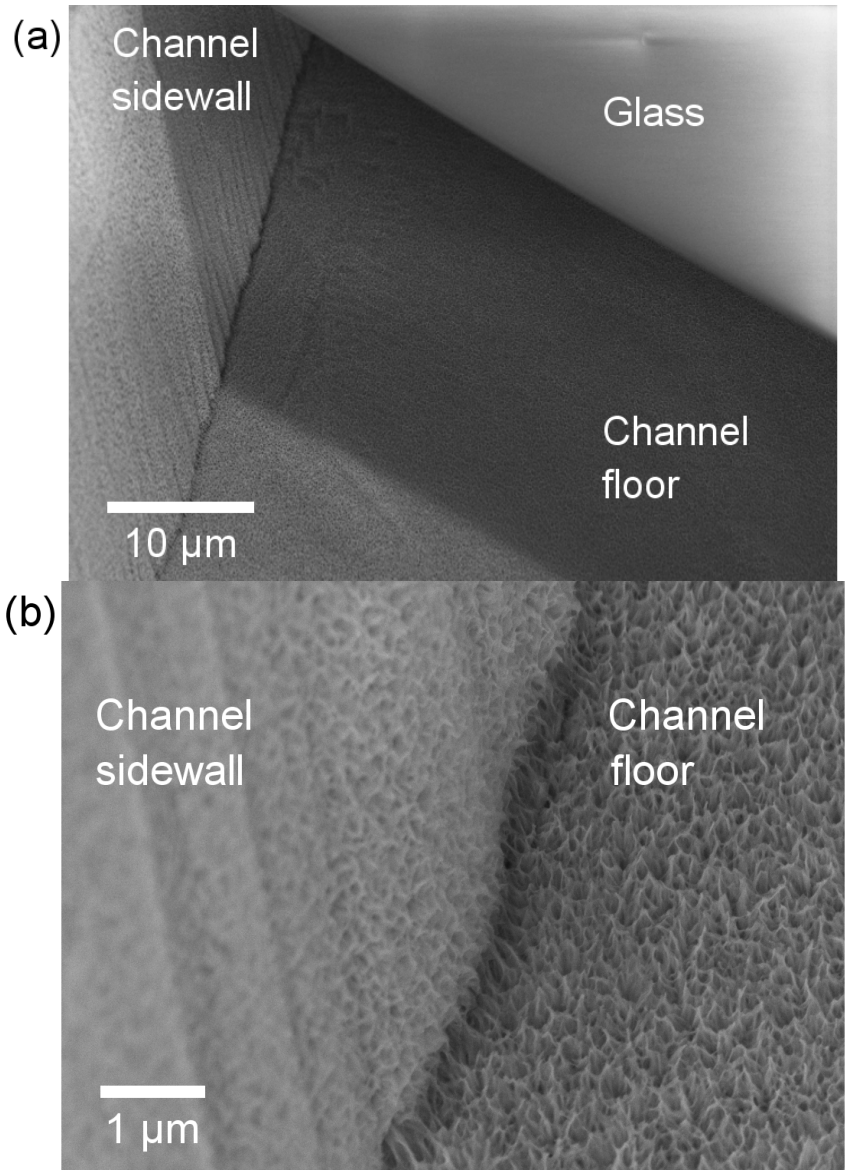

Figure 4-10. Scanning electron micrographs showing monolithic integration of NPT within an anodically bonded Ti/N-BK7 microfluidic device via aqueous H_2O_2 oxidation: a) Low-magnification; b) High-magnification.

4.4. Conclusion

We have demonstrated the first anodic bonding process capable of successfully bonding bulk Ti and glass substrates at the wafer-scale without adhesives or interlayers. Using this process, we have shown that: (a) bond strengths exceeding the strength of the glass can be achieved at temperatures as low as 250°C; (b) when combined with our existing Ti DRIE capability, functional Ti/glass-based microfluidic devices can be fabricated at the wafer-scale; and (c) NPT can be easily integrated within such devices using an aqueous H_2O_2 oxidation process. Collectively, this demonstrates the promise embodied in Ti anodic bonding for leveraging the advantageous properties of Ti for fabrication of optically accessible microfluidic devices with enhanced robustness, performance, and functionality. Furthermore, this work illustrates the specific potential afforded by the combination of Ti anodic bonding, Ti DRIE, and H_2O_2-based NPT growth for future realization of robust, high-performance microreactors for photocatalysis applications.

5 CONCLUSIONS

The fabrication of Ti MNs with through-thickness fenestrations that serve as reservoirs for drug storage is demonstrated. Devices designs with widths ranging from 50 – 200 μm, a fixed thickness of 50 μm, lengths ranging from 500 – 1500 μm, and a fixed needle tip angle of 60° are shown. FEA simulations of the fenestrated Ti MNs have been shown to be in good agreement with mechanical testing results, suggesting there is room for future MN design optimization. Axial compression of the fenestrated MNs showed that devices fail gracefully without fracture or fragmentation, suggesting that Ti MNs may provide a safer means for ocular delivery relative to other devices fabricated from Si or glass. Moreover, uniform deposition of a fast-dissolving model drug coating formulation has been demonstrated. Coating evaluations found that fenestrated MNs are capable of increasing drug-loading capacity by 5-fold, relative to solid MN geometries of identical shank dimension. These findings demonstrate that fenestrated MNs can provide a means minimizing the number of MNs required for delivering therapeutically relevant doses. Finally, results from insertion studies in excised rabbit cornea corroborate many of these findings by demonstrating capability for reliable MN insertion and drug delivery with enhanced sub-surface drug delivery. Collectively, these results begin to demonstrate the potential embodied in fenestrated Ti MNs for providing a safe, simple, and efficacious means for ocular drug delivery.

The first anodic bonding process capable of successfully bonding bulk Ti and glass substrates at the wafer-scale without adhesives or interlayers has been demonstrated. Bond strengths exceeding the strength of the glass were achieved at temperatures as low as 250°C. By combining our Ti DRIE capability, functional Ti/glass-

based microfluidic devices were fabricated at the wafer-scale. We showed that NPT can be easily integrated within such devices using an aqueous H_2O_2 oxidation process. Collectively, this demonstrates the promise embodied in Ti anodic bonding for leveraging the advantageous properties of Ti for fabrication of optically accessible microfluidic devices with enhanced robustness, performance, and functionality. Furthermore, this work illustrates the specific potential afforded by the combination of Ti anodic bonding, Ti DRIE, and H_2O_2-based NPT growth for future realization of robust, high-performance microreactors for photocatalysis applications. Together, these results demonstrate the the use of Ti MEMS technology for the fabricating novel drug delivery and microfluidic systems with enhanced robustness, safety, and performance.

5.1. Recommendations for Future Work Ti Microneedle Work

MNs developed in this dissertation were fabricated as single needle devices, however, Ti DRIE provides capabilities for designing MNs with a variety of geometries. For example, planar arrays of fenestrated MNs can be made. Bonding techniques can be explored for stacking substrates, thereby enabling the fabrication of highly-dense MN arrays. Another technique for fabricating MN arrays would be to etch planar geometries on a substrate, then selectively bend the MNs shanks out-of-plane. This method provides a more simple means for fabricating MN arrays, and has been demonstrated on similar geometry devices made from stainless steel (Gill and Prausnitz 2008).

MN coatings developed in this dissertation were based on aqueous drug formulations. The fenestrated Ti MNs demonstrated capabilities to provide a protective

cavity for delivering drugs in the sub-surface tissue. These results motivate the exploration of the potential for use of fenestrated MNs with nano- or microparticle-entrained MN coatings, since this may provide opportunity for achieving sustained delivery, and thus, reduced treatment frequency.

Coating evaluations in this dissertation focused on qualitative assessments and did not explore in detail the wetting of individual fenestrations. This is in large part due to the limitations of using fluorescence microscopy to evaluation fenestration filling. Confocal microscopy provides one method for imaging individual fenestration fillings. Confocal microscopy can be used to capture three-dimensional images of the coated fenestrated MNs. Using imaging software techniques, cross sections show the meniscuses formed by the coating formulation, which can be used to calculate unfilled volumes and estimate fenestration fillings.

5.2. Recommendations for Future Work Ti Microfluidic Work

The future use of Ti anodic bonding for photocatalysis applications requires an in-depth study of NPT. As such, recommendations for future work include a thorough design of experiments to understand NPT photocatalytic degradation efficiencies. Studies to using NPT films to degrade methylene blue solutions would provide insight into optimization of NPT devices for water purification. NPT growth conditions and morphologies and their corresponding effects on degradation efficiencies should be explored.

Furthermore, the ability to use Ti DRIE to fabricate pillars or posts within microfluidic channels provides potential for further enhancing degradation efficiencies

when integrated into a device. Microfabricated posts with NPT can provide increased surface area for enhanced efficiencies. Additionally, the integration of such features provides opportunity for use in filtration applications.

BIBLIOGRAPHY

Ahsan, Syed Saad, Abdurrahman Gumus, and David Erickson. 2013. "Redox Mediated Photocatalytic Water-Splitting in Optofluidic Microreactors." *Lab on a Chip* 13 (3): 409. doi:10.1039/c2lc41129f.

Bai, Qing, Kensall D. Wise, and David J. Anderson. 2000. "A High-Yield Microassembly Structure for Three-Dimensional Microelectrode Arrays." *Biomedical Engineering, IEEE Transactions on* 47 (3): 281–89.

Briand, Danick, Patrick Weber, and Nicolaas F. de Rooij. 2004. "Bonding Properties of Metals Anodically Bonded to Glass." *Sensors and Actuators A: Physical* 114 (2-3): 543–49. doi:10.1016/j.sna.2003.10.070.

Bustillo, James M., Roger T. Howe, and Richard S. Muller. 1998. "Surface Micromachining for Microelectromechanical Systems." *Proceedings of the IEEE* 86 (8): 1552–74.

Castellana, Edward T., Sho Kataoka, Fernando Albertorio, and Paul S. Cremer. 2006. "Direct Writing of Metal Nanoparticle Films Inside Sealed Microfluidic Channels." *Analytical Chemistry* 78 (1): 107–12. doi:10.1021/ac051288j.

Chen, Yih-Fan, Li Jiang, Matthew Mancuso, Aadhar Jain, Vlad Oncescu, and David Erickson. 2012. "Optofluidic Opportunities in Global Health, Food, Water and Energy." *Nanoscale* 4 (16): 4839. doi:10.1039/c2nr30859b.

Ciolino, J. B., T. R. Hoare, N. G. Iwata, I. Behlau, C. H. Dohlman, R. Langer, and D. S. Kohane. 2009. "A Drug-Eluting Contact Lens." *Investigative Ophthalmology & Visual Science* 50 (7): 3346–52. doi:10.1167/iovs.08-2826.

Ciolino, Joseph B., Cristina F. Stefanescu, Amy E. Ross, Borja Salvador-Culla, Priscila Cortez, Eden M. Ford, Kate A. Wymbs, et al. 2014. "In Vivo Performance of a Drug-Eluting Contact Lens to Treat Glaucoma for a Month." *Biomaterials* 35 (1): 432–39. doi:10.1016/j.biomaterials.2013.09.032.

Davis, Shawn P, Benjamin J Landis, Zachary H Adams, Mark G Allen, and Mark R Prausnitz. 2004. "Insertion of Microneedles into Skin: Measurement and Prediction of Insertion Force and Needle Fracture Force." *Journal of Biomechanics* 37 (8): 1155–63. doi:10.1016/j.jbiomech.2003.12.010.

Davis, S.P., W. Martanto, M.G. Allen, and M.R. Prausnitz. 2005. "Hollow Metal Microneedles for Insulin Delivery to Diabetic Rats." *IEEE Transactions on Biomedical Engineering* 52 (5): 909–15. doi:10.1109/TBME.2005.845240.

Di Giovanni, M. 1982. *Flat and Corrugated Diaphragm Design Handbook*. New York: Marcel Dekker.

Ding, Changsong, Gaurav Soni, Payam Bozorgi, Brian D. Piorek, Carl D. Meinhart, and Noel C. MacDonald. 2010. "A Flat Heat Pipe Architecture Based on Nanostructured Titania." *Journal of Microelectromechanical Systems* 19 (4): 878–84. doi:10.1109/JMEMS.2010.2051019.

Emily R. Parker, Brian J. Thibeault, Marco F. Aimi, Masaru P. Rao, and Noel C. MacDonald. 2005. "Inductively Coupled Plasma Etching of Bulk Titanium for MEMS Applications." *Journal of Electrochemical Society* 152 (10): C675–83.

Erickson, David, David Sinton, and Demetri Psaltis. 2011. "Optofluidics for Energy Applications." *Nature Photonics* 5 (10): 583–90. doi:10.1038/nphoton.2011.209.

ER Parker, MP Rao, KL Turner, CD Mienhart, and NC MacDonald. 2007. "Bulk Micromachined Titanium Microneedles." *MIcroelectromechanical Systems* 16 (2): 289–95.

Falavarjani, K. Ghasemi, and Q. D. Nguyen. 2013. "Adverse Events and Complications Associated with Intravitreal Injection of Anti-VEGF Agents: A Review of Literature." *Eye* 27 (7): 787–94.

Fujishima, A, X Zhang, and D Tryk. 2008. "TiO2 Photocatalysis and Related Surface Phenomena." *Surface Science Reports* 63 (12): 515–82. doi:10.1016/j.surfrep.2008.10.001.

Gan, Li, Jing Wang, Min Jiang, Hanah Bartlett, Defang Ouyang, Frank Eperjesi, Jianping Liu, and Yong Gan. 2013. "Recent Advances in Topical Ophthalmic Drug Delivery with Lipid-Based Nanocarriers." *Drug Discovery Today* 18 (5-6): 290–97. doi:10.1016/j.drudis.2012.10.005.

Gaudana, Ripal, J. Jwala, Sai H. S. Boddu, and Ashim K. Mitra. 2009. "Recent Perspectives in Ocular Drug Delivery." *Pharmaceutical Research* 26 (5): 1197–1216. doi:10.1007/s11095-008-9694-0.

Gensler, Heidi, Roya Sheybani, Po-Ying Li, Ronalee Lo Mann, and Ellis Meng. 2012. "An Implantable MEMS Micropump System for Drug Delivery in Small Animals." *Biomedical Microdevices* 14 (3): 483–96. doi:10.1007/s10544-011-9625-4.

Gerhard, Welsch, R. Boyer, and E.W. Collings. 1994. *Materials Properties Handbook: Titanium Alloys*. Ohio: ASM International.

Gill, Harvinder S., and Mark R. Prausnitz. 2007a. “Coated Microneedles for Transdermal Delivery.” *Journal of Controlled Release* 117 (2): 227–37. doi:10.1016/j.jconrel.2006.10.017.

———. 2007b. “Coating Formulations for Microneedles.” *Pharmaceutical Research* 24 (7): 1369–80. doi:10.1007/s11095-007-9286-4.

———. 2008. “Pocketed Microneedles for Drug Delivery to the Skin.” *Journal of Physics and Chemistry of Solids* 69 (5-6): 1537–41. doi:10.1016/j.jpcs.2007.10.059.

Gorges, Roger, Susann Meyer, and Günter Kreisel. 2004. “Photocatalysis in Microreactors.” *Journal of Photochemistry and Photobiology A: Chemistry* 167 (2-3): 95–99. doi:10.1016/j.jphotochem.2004.04.004.

Henry, Sebastien, Devin V. McAllister, Mark G. Allen, and Mark R. Prausnitz. 1998. “Microfabricated Microneedles: A Novel Approach to Transdermal Drug Delivery.” *Journal of Pharmaceutical Sciences* 87 (8): 922–25.

Hoogerwerf, Arnold C., and K. D. Wise. 1994. “A Three-Dimensional Microelectrode Array for Chronic Neural Recording.” *Biomedical Engineering, IEEE Transactions on* 41 (12): 1136–46.

Järvinen, Kristiina, Tomi Järvinen, and Arto Urtti. 1995. “Ocular Absorption Following Topical Delivery.” *Advanced Drug Delivery Reviews* 16 (1): 3–19.

J Jiang, HS Gill, D Ghate, BE McCarey, SR Patel, HF Edelhauser, and MR Prausnitz. 2007. “Coated Microneedles for Drug Delivery to the Eye.” *Investigative Ophthalmology & Visual Science* 48: 4038–43.

J Jiang, JS Moore, HF Edelhauser, and MR Prausnitz. 2009. “Intrascleral Drug Delivery to the Eye Using Hollow Microneedles.” *Pharmaceutical Research* 26: 395–403.

Kim, Yoo C., Henry F. Edelhauser, and Mark R. Prausnitz. 2014. “Targeted Delivery of Antiglaucoma Drugs to the Supraciliary Space Using Microneedles.” *Investigative Ophthalmology & Visual Science* 55 (11): 7387–97.

Kim, Yoo C., Hans E. Grossniklaus, Henry F. Edelhauser, and Mark R. Prausnitz. 2014. “Intrastromal Delivery of Bevacizumab Using Microneedles to Treat Corneal Neovascularization.” *Investigative Ophthalmology & Visual Science* 55 (11): 7376–86.

K. M. Knowles, and A. T. J. van Helvoort. 2006. “Anodic Bonding.” *International Materials Review* 51 (5): 273–311.

Lei, Lei, Ning Wang, X. M. Zhang, Qidong Tai, Din Ping Tsai, and Helen L. W. Chan. 2010. "Optofluidic Planar Reactors for Photocatalytic Water Treatment Using Solar Energy." *Biomicrofluidics* 4 (4): 043004. doi:10.1063/1.3491471.

Lo, Ronalee, Po-Ying Li, Saloomeh Saati, Rajat N. Agrawal, Mark S. Humayun, and Ellis Meng. 2009. "A Passive MEMS Drug Delivery Pump for Treatment of Ocular Diseases." *Biomedical Microdevices* 11 (5): 959–70. doi:10.1007/s10544-009-9313-9.

Madou, Mark J. 2002. *Fundamentals of Microfabrication: The Science of Miniaturization*. 2nd ed. Taylor & Francis.

Marco F. Aimi, Masaru P. Rao, Noel C. MacDonald, Abu Samah Zuruzi, and David P. Bothman. 2004. "High-Aspect-Ratio Bulk Micromachining of Titanium." *Nature Materials* 3 (February): 103–5.

Matsushita, Yoshihisa, Shinji Kumada, Kazuhito Wakabayashi, Kosaku Sakeda, and Teijiro Ichimura. 2006. "Photocatalytic Reduction in Microreactors." *Chemistry Letters* 35 (4): 410–11.

Matthews, A., C. Hutnik, K. Hill, T. Newson, T. Chan, and G. Campbell. 2014. "Indentation and Needle Insertion Properties of the Human Eye." *Eye*. http://www.nature.com/eye/journal/vaop/ncurrent/full/eye201499a.html.

McCarthy, Patrick T., Kevin J. Otto, and Masaru P. Rao. 2011. "Robust Penetrating Microelectrodes for Neural Interfaces Realized by Titanium Micromachining." *Biomedical Microdevices* 13 (3): 503–15. doi:10.1007/s10544-011-9519-5.

Nagai, Hidenori, Takashi Irie, Junko Takahashi, and Shin-ichi Wakida. 2007. "Flexible Manipulation of Microfluids Using Optically Regulated Adsorption/desorption of Hydrophobic Materials." *Biosensors and Bioelectronics* 22 (9-10): 1968–73. doi:10.1016/j.bios.2006.08.037.

Ninghao, Jiang. 2006. "Ocular Drug Delivery Using Microneedles." Georgia Institute of Technology.

Ning Wang, Xuming Zhang, Yun Wang, Weixing Yu, and Helen L. W. Chan. 2013. "Microfluidic Reactors for Photocatalytic Water Purification." *Lab on a Chip* 14 (December): 1074–82.

Ohring, M. 1992. "The Materials Science of Thin Films." In , 418–19. San Diego, CA: Academic Press.

Osterberg, Lars, and Terrence Blaschke. 2005. "Adherence to Medication." *New England Journal of Medicine* 353 (5): 487–97.

Patel, Ashaben. 2013. “Ocular Drug Delivery Systems: An Overview.” *World Journal of Pharmacology* 2 (2): 47. doi:10.5497/wjp.v2.i2.47.

Patel, Samirkumar R., Damian E. Berezovsky, Bernard E. McCarey, Vladimir Zarnitsyn, Henry F. Edelhauser, and Mark R. Prausnitz. 2012. “Targeted Administration into the Suprachoroidal Space Using a Microneedle for Drug Delivery to the Posterior Segment of the Eye.” *Investigative Ophthalmology & Visual Science* 53 (8): 4433–41.

Patel, Samirkumar R., Angela S. P. Lin, Henry F. Edelhauser, and Mark R. Prausnitz. 2011. “Suprachoroidal Drug Delivery to the Back of the Eye Using Hollow Microneedles.” *Pharmaceutical Research* 28 (1): 166–76. doi:10.1007/s11095-010-0271-y.

Prausnitz, Mark R. 2004. “Microneedles for Transdermal Drug Delivery.” *Advanced Drug Delivery Reviews* 56 (5): 581–87. doi:10.1016/j.addr.2003.10.023.

Pulido, J. S., M. E. Zobitz, and K. N. An. 2006. “Scleral Penetration Force Requirements for Commonly Used Intravitreal Needles.” *Eye* 21 (9): 1210–11.

Saliterman, Steven. 2006. *Fundamentals of BioMEMS and Medical Microdevices*. 1st ed. SPIE Publications.

Shima, Chiharu, Hirokazu Sakaguchi, Fumi Gomi, Motohiro Kamei, Yasushi Ikuno, Yusuke Oshima, Miki Sawa, Motokazu Tsujikawa, Shunji Kusaka, and Yasuo Tano. 2008. “Complications in Patients after Intravitreal Injection of Bevacizumab.” *Acta Ophthalmologica* 86 (4): 372–76. doi:10.1111/j.1600-0420.2007.01067.x.

Shott North America. 2004. “TIE-33: Design Strength of Optical Glass and ZERODUR.”

Shu, Qiong, Juan Su, Gang Zhao, Ying Wang, and Jing Chen. 2008. “Evaluation and Characterization of Titanium to Glass Anodic Bonding.” In *2008 Second International Conference on Integration and Commercialization of Micro and Nanosystems*, 597–600. American Society of Mechanical Engineers. http://proceedings.asmedigitalcollection.asme.org/proceeding.aspx?articleid=1623035.

SR Patel, ASP Lin, HF Edelhauser, and MR Prausnitz. 2011. “Suprachoroidal Drug Delivery to the Back of the Eye Using Hollow Microneedles.” *Pharmaceutical Research* 28: 166–76.

Takei, G, T Kitamori, and H Kim. 2005. “Photocatalytic Redox-Combined Synthesis of -Pipecolinic Acid with a Titania-Modified Microchannel Chip.” *Catalysis Communications* 6 (5): 357–60. doi:10.1016/j.catcom.2005.02.010.

The Eye Diseases Prevalence Research Group. 2004. “Prevalence of Age-Related Macular Degeneration in the United States.” *Arch Ophthalmol* 122 (4): 564–72.

Toyoda, M, Y Fujiya, M Nayama, and T Yamada. 1993. “Study on Glass-Metal Bonding by Anodic Bonding.” *Quarterly Journal of the Japan Welding Society 11* 1: 208–2013.

Urtti, Arto. 2006. “Challenges and Obstacles of Ocular Pharmacokinetics and Drug Delivery.” *Advanced Drug Delivery Reviews* 58 (11): 1131–35. doi:10.1016/j.addr.2006.07.027.

Vandrangi, Prashanthi, Shannon C. Gott, Ryan Kozaka, Victor G. J. Rodgers, and Masaru P. Rao. 2014. “Comparative Endothelial Cell Response on Topographically Patterned Titanium and Silicon Substrates with Micrometer to Sub-Micrometer Feature Sizes.” Edited by Dario Pisignano. *PLoS ONE* 9 (10): e111465. doi:10.1371/journal.pone.0111465.

Van Helvoort, A. T. J., K. M. Knowles, R. Holmestad, and J. A. Fernie. 2004. “Anodic Oxidation during Electrostatic Bonding.” *Philosophical Magazine* 84 (6): 505–19. doi:10.1080/14786430310001637015.

Varma, Rohit, Paul P. Lee, Ivan Goldberg, and Sameer Kotak. 2011. “An Assessment of the Health and Economic Burdens of Glaucoma.” *American Journal of Ophthalmology* 152 (4): 515–22. doi:10.1016/j.ajo.2011.06.004.

Wallis, G. 1970. “Direct-Current Polarization During Field-Assisted Glass-Metal Sealing.” *Journal of the American Ceramic Society* 53 (10): 563–67.

Wallis, George. 1969. “Field Assisted Glass-Metal Sealing.” *Journal of Applied Physics* 40 (10): 3946. doi:10.1063/1.1657121.

Wallis, George, J Dorsey, and J Beckett. 1971. “Field Assisted Seals of Glass to Fe-Ni-Co Alloy.” *American Ceramic Society Bulletin* 50 (12): 958–61.

Wong, Wan Ling, Xinyi Su, Xiang Li, Chui Ming G. Cheung, Ronald Klein, Ching-Yu Cheng, and Tien Yin Wong. 2014. “Global Prevalence of Age-Related Macular Degeneration and Disease Burden Projection for 2020 and 2040: A Systematic Review and Meta-Analysis.” *The Lancet Global Health* 2 (2): e106–16.

Zhang, Y. T., F. Bottausci, M. P. Rao, E. R. Parker, I. Mezic, and N. C. MacDonald. 2008. “Titanium-Based Dielectrophoresis Devices for Microfluidic Applications.” *Biomedical Microdevices* 10 (4): 509–17. doi:10.1007/s10544-007-9159-y.

Zuruzi, Abu Samah, Hannah C. Gardner, Adam J. Monkowski, and Noel C. MacDonald. 2013. “Tailored Nanostructured Titania Integrated on Titanium Micropillars with Outstanding Wicking Properties.” *Lab on a Chip* 13 (12): 2414. doi:10.1039/c3lc50098e.

Zuruzi, A. S., and N. C. MacDonald. 2005. “Facile Fabrication and Integration of Patterned Nanostructured TiO2 for Microsystems Applications.” *Advanced Functional Materials* 15 (3): 396–402. doi:10.1002/adfm.200400135.

APPENDIX

Appendix A – Substrate Preparation

Cleaning procedures and substrate preparation techniques are crucial to the successful creation of the devices discussed in this dissertation. Particular care is required for successful anodically bonded devices, as particle contamination can be a beast. As such, it is recommended that a clean smock is worn while processing devices, in addition to clean a face mask, hair cap, and gloves.

Titanium Foils (Fenestrated Ti MNs)

1. Using sharp scissors, cut 50 μm Ti foils to approximately 1 ¼" x 1 ¼".
2. Using clean glassware and a high intensity, high frequency ultrasonic agitation bath, subsequently clean the Ti foils using isopropanol (IPA), acetone (ACE), and DI water, for 3 min each. From this point forward, this solvent cleaning process will be abbreviated as 3/3/3 cleaning process.
3. Following 3/3/3 cleaning, dry the foils using a N_2 air gun and place them on a clean hotplate at 115°C for 5 min for a dehydration bake, ensuring that all moisture is removed from the samples.
4. Following the dehydration bake, transfer the Ti foils to a clean sample carrier and store for subsequent processing.

Silicon Carriers (Fenestrated Ti MNs)

1. Using a diamond scribe, cut a single sided polished (SSP) Si wafer to approximately 1" x 1" pieces.
2. Clean the Si pieces using the 3/3/3 cleaning process, followed by N_2 drying and dehydration baking at 115 °C for 5 min.
3. Transfer the Si pieces to a clean sample carrier and store for subsequent processing.

Titanium Wafers (Ti Anodic Bonding)

1. Peel off the protective film from the polished side of a new SSP Ti wafer.
2. Clean the wafer using the 3/3/3 cleaning process. If the wafer being cleaned is intended for immediate bonding (i.e., there is no intention to etch features on the substrate), then allow the wafer to remain immersed in the DI water until ready for bonding. If features are to be etched on the substrate, proceed to step 3
3. Following 3/3/3 cleaning, dry the wafer using a N_2 air gun and place it on a clean hotplate at 115°C for 5 min to dehydration.
4. Transfer the Ti foil to a clean wafer carrier and store for subsequent processing.

N-BK7 Wafers (Ti Anodic Bonding)

1. Clean the wafer using the 3/3/3 cleaning process, however, reduce the intensity of the ultrasonic agitation bath to low. Reducing the agitation intensity minimizes the potential risk for breaking the wafer during the cleaning process.

2. Allow the wafer to remain immersed in the DI water until ready for bonding.

Appendix B – Deposition (ICP PECVD)

Etching of Ti requires the use of a hard mask due to inadequate etch selectivity associated with using photoresist masks, as well as the potential for photoresist to cause issues such as micromasking, a.k.a. grassing, during the plasma etch process. Deposition of a SiO_2 hard mask was performed using an ICP PECVD tool (VLR, Unaxis, St. Petersburg, FL; Process conditions: 15 mT chamber pressure, 400 W ICP source power, 5 W substrate power, 5.9 sccm 100% SiH_4, 20 sccm Ar, 10 sccm O_2, and 100°C lower electrode temperature).

Titanium Foils (Fenestrated Ti MNs)

1. Place previously cleaned Ti foils on a silicon carrier wafer, allowing approximately 5 mm clearance from the perimeter of the wafer to ensure reliable operation of the tools mechanical clamp mechanism during the deposition process. Depending on the cut foil dimensions, a 4" Si carrier is able to mount 4 to 5 foils per deposition process. There is no need to adhere the foils to the carrier wafer (e.g., using mounting tape, foil, or grease).
2. Using the above process, deposit 2.5 μm of SiO_2 on the surface.

Appendix C – Lithography

To ensure uniformity and consistency for lithography using flexible thin foil Ti, a technique for mounting foils to a flat hard surface was necessary. Processing Ti foils was made possible by mounting with double-sided thermally conductive adhesive tape and flat Si carrier chips. As previously discussed, Ti foils were cut slightly larger than the Si carriers, allowing the inherent bow of the foils to hang down over the edges of the Si carrier when mounted concave down, thereby enabling uniform contact of the substrate surface with the quartz photomask when performing hard or vacuum contact lithography.

Ti wafers processed for anodic bonding of BPT specimens and microfluidic devices utilized an SU-8 resist mask. Through the development of the anodic bonding process, it was determined that an SiO_2 hard mask to deep etch Ti wafers provided a means for successful Ti DRIE, however, the process of removing residual oxide from the Ti surface via dry etching resulted in micron-scale roughening of the Ti surface which adversely affected the quality of subsequent bonding with N-BK7. This surface roughening, although not detectable by eye, consistently caused inconsistent, poor quality bonding with N-BK7, as seen from the incomplete or lack of uniformity across the entirety of the bonded stack. Unlike a deposited hard mask, SU-8 can be completely removed using conventional photoresist strippers that are compatible with Ti and cause no damage to the substrate surface. Furthermore, the use of an SU-8 mask simplifies the process of fabricating Ti microfluidic devices by eliminating the necessity to deposit oxide using a PECVD tool, as well as removing two additional plasma etch steps (i.e., no longer requiring an oxide etch mask or residual oxide removal etch).

Titanium Foils (Fenestrated Ti MNs)

1. In preparation for resist spinning and lithography, clean oxide coated foils using the 3/3/3 cleaning process, followed by N_2 drying, and dehydration baking at 115°C for 5 min.
2. Lightly adhere the tacky side of a strip of double-sided thermally conductive adhesive tape (9882, 3M, St. Paul, MN) to a previously cleaned Si carrier chip. Using a flat, rectangular tipped tweezer, apply gentle, uniform pressure in a back-and-forth manner to the tape, beginning in the center and working outward radially. Make sure to avoid trapping any air pockets or bubbles between the tape and the chip. If air bubbles under the tape are noticed, remove the tape using a razor blade and repeat the mounting using a fresh strip of tape until no bubbles are visible. Using a razor blade, cut off excess tape hanging over the perimeter of the Si carrier.
3. Remove the protective clear film from the tape mounted Si carrier to expose the adhesive. With a non-shedding wipe, firmly press the foil down on to the adhesive chip, starting at the edge and utilizing rolling motion to reduce the risk of entrapping air bubbles between the tape and the foil.
4. Bake the mounted foil substrate on a hotplate at 115°C for 5 min to promote adhesion between the foil and the carrier.
5. Perform an O_2 plasma clean (Technics/PE-IIA) on the substrate for 1 min at 100 W substrate power and 300 mT chamber pressure.

6. Place a new, clean wipe in a resist coating spinner and choose an appropriately sized vacuum chuck for the substrate dimensions.
7. Place the substrate in the center of the chuck and apply vacuum to the substrate.
8. Use an N_2 gun to blow off the surface of the substrate, then activate the spin cycle to allow any remaining particulates to be removed from the substrate surface.
9. Spin HMDS at 3500 rpm for 45 sec.
10. Allow HMDS vapors to dissipate for 1 min.
11. Dispense SPR220-7.0 (Shipley) over the substrate allow it to sit for 30 sec.
12. Spin the resist at 3500 rpm for 45 sec.
13. Soft bake at 115°C for 90 sec.
14. Let stand for 35 min.
15. Develop using AZ300MIF for 70 sec.
16. Store substrate for subsequent processing.

Titanium Wafers (Ti Anodic Bonding)

1. Perform an O_2 plasma clean (Technics/PE-IIA) on the substrate for 1 min at 100 W substrate power and 300 mT chamber pressure.
2. Place a new, clean wipe in a resist coating spinner and choose an appropriately sized vacuum chuck for the wafer dimensions.
3. Place the wafer in the center of the chuck and apply vacuum.
4. Use an N_2 gun to blow off the surface of the wafer, then activate the spin cycle to allow any remaining particulates to be removed from the substrate surface.

5. Once the spin cycle has completed, use a clean pipet to dispense OmniCoat (MicroChem) on the entire surface of the substrate and allow it to sit for 30 sec.
6. Spin the OmniCoat at 3500 rpm for 45 sec.
7. Bake for 1 min at 200°C and let cool.
8. Place the wafer in the center of the resist coating spinner's chuck and apply vacuum. Dispense SU-8 2075 (MicroChem) onto the center of the wafer by pouring directly from the bottle. It is not necessary to pour resist over the entire wafer.
9. Cut the top end of a large plastic pipette (the tube end used for suctioning), and use it to carefully spread the SU-8 outward over the wafer. This method works best for minimizing the potential for bubbles or inconsistencies to form in the resist.
10. Spin the SU-8 at 3500 rpm for 45 sec.
11. Soft bake for 9 min at 65°C and let cool.

Appendix D – Titanium DRIE

All Ti etching was performed using a E640-ICP (Panasonic Factory Solutions, Osaka, Japan). Baseline process conditions for Ti etching were 15 mT chamber pressure, 400 W ICP source power, 100 W substrate power, 100 sccm Cl_2, 5 sccm Ar. Through the development of the Ti MN work, it was that adding 1 sccm O_2 helped increase the sidewall passivation, thereby creating smoother sidewall profiles. Adding any more than 1 sccm O_2 caused micromasking.

For the development of the Ti anodic bonding work, the baseline Ti DRIE recipe was found to cause micromasking of the etched features. I believed this was caused by a change in the etch chemistry while using SU-8 as an etch mask, rather than SiO_2. Increasing the substrate power to 200 W was found to improve etching. Doing so reduced the potential for overpassivation during the etch caused by SU-8 and Ti etched radicals.

Appendix D – Wafer Bonding and Dicing

Wafer Bonding

Particle contamination plays a critical role in resulting bond quality, and as such, special cleaning procedures were implemented to ensure contaminants were minimized. All wafer preparation was conducted at the cleanroom solvent bench with exhaust system nearest to the wafer bonder tool. A new face mask, hair cap, and pair of gloves were always worn when preparing wafers for bonding. Glassware was rinsed and drained with solution at minimum two times before preparing a fresh solution for cleaning. Wafer handling tweezers were cleaned by sequential agitation in acetone, isopropanol and DI water prior to handling wafers. Following glassware and tweezer cleaning, a single Ti wafer was cleaned by sequential ultrasonic agitation in acetone, isopropanol, and DI water for 3 min each, then allowed to remain submerged in the DI water until further processing. Using separate glassware that had undergone the same aforementioned cleaning procedure, a single N-BK7 wafer was then cleaned using the same acetone/isopropanol/DI water (3/3/3) ultrasonic agitation procedure, and also left submerged in the DI water. At this point, gloves were again replaced with a new pair, and two new sets of absorbent cleanroom wipes were laid out on the benchtop with adequate spacing between them. Two new sets of new non-shedding cleanroom wipes were then placed on top of the previously laid out absorbent wipes. Using clean wafer tweezers, the Ti wafer was then removed from the DI water solution and placed on one of the non-shedding wipe stacks, and was immediately followed by N_2 drying. Particular care was taken during N_2 drying to observe that the wafer surface was free of particle contaminants

or debris. If for any reason particle contaminants could not be removed from the substrate surface during N_2 drying, the wafer was immediately submerged in a fresh DI water solution and allowed to undergo 3 min of ultrasonic agitation prior to attempting the N_2 drying step again. Once the Ti wafer surface was deemed clean enough for bonding, a clean, dry, glassware container was placed over the top of the wafer to ensure that particle contamination would be minimized while the same procedure N_2 drying procedure was applied to the N-BK7 wafer. Finally, when both wafers were appropriately cleaned and deemed suitable for bonding, the dried surfaces of the substrates were manually placed in contact with the major flats providing consistent orientation. The wafer stack was then immediately loaded into a commercial wafer bonder (SB6-E, SUSS MicroTec, Germany) and bonded under the following process conditions: temperatures ranging from 200 to 400°C; 300 V applied voltage; 5E−3 mbar chamber pressure, 225 mbar tool force, and 3 min bond time.

Wafer Dicing

Dicing bonded Ti/N-BK7 wafers is an important step toward the development of scalable microfluidic devices, and therefore reproducibility is important for maximizing device yield from a single wafer. Wafer dicing was performed using a 7100 Series Dicing Saw (Advanced Dicing Technologies, Horsham, PA). Using a 2.050-8C-54RU blade and 52 mm hub provided the largest and thickest blade, which assisted in cutting through bonded stacks. To successfully dice Ti/glass wafers, it is important to mount the substrate with the glass side up, i.e., the blade comes in contact with the glass first. Doing so helps

the blade “clean” itself, which is necessary due to the difficult nature of dicing Ti. Along with lower cutting speeds (~1 mm/s), it was possible to dice bonded wafer stacks

Appendix E – Miscellaneous Methods

Rabbit Eye Dissection

1. Acquire a rabbit eye for dissection and place in a clean, disposable container with PBS.
2. Use a combination of sharp razor blades and tweezers to dissect the eye at the sclera around the cornea.
3. Drain the vitreous and remove the lens.
4. Cut the cornea into ~4 mm width slices and set aside in a sealed PBS solution.
5. Store extra samples in a biohazard-safe refrigerator.
6. Dispose of all remaining unused tissues, contaminated wipes, and blades in corresponding biological waste storage bag or sharps containers and mark for proper disposal.

MN Penetration and Histological Sectioning

1. Turn on the cryostat and allow the system to cool to -20°C.
2. Dispense a thin, uniform layer of optimal cutting fluid (OCT) on a sample mount and allow for it to freeze.
3. Place a slice of cornea on a clean wipe.
4. Pat dry the cornea with a wipe.
5. Using tweezers, carefully penetrate the cornea using a coated MN perpendicular to the surface of the tissue, and hold for 1 min.
6. Remove the MN and set aside.

7. Apply a thin layer of OCT on the frozen sample mount, then lay the cornea on top.
8. Continue to apply OCT to the tissue as the OCT freezes. This might take a while depending on the size of the sample.
9. Once completely frozen in OCT, the frozen block containing the cornea sample must be rotated 90 degrees to collect cross sections of the MN penetration site. Using a razor, pry off the frozen sample, then proceed to remount it at a 90 degree orientation. Continue this process until the sample is ready to be sectioned.

Appendix F – Figures

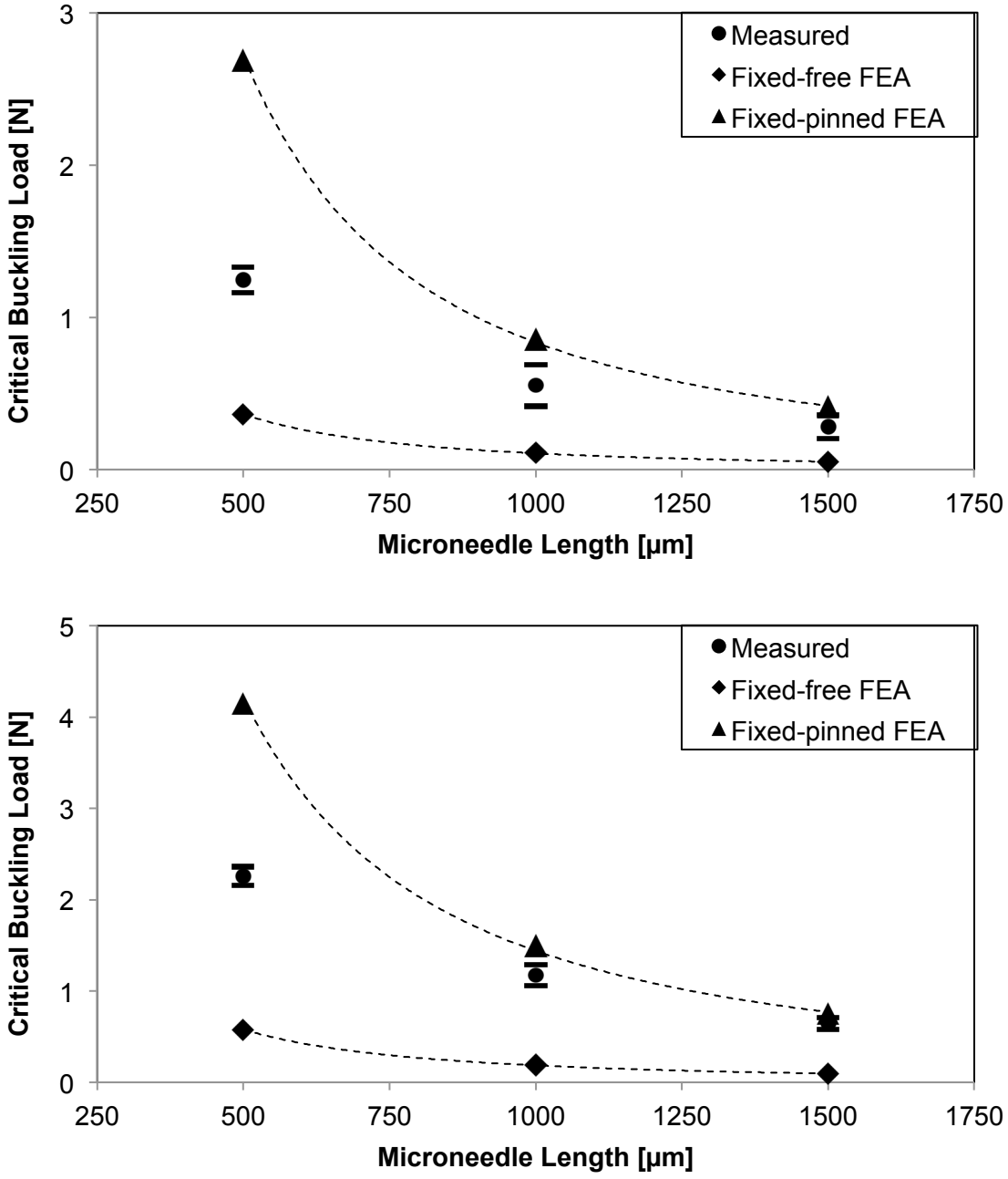

Figure F-1. Measured and FEA-predicted critical buckling loads for solid Ti MNs with varying µm width, 50 µm thickness, and 500 - 1500 µm lengths: a) 50 µm width; b) 100 µm width. Experimental data points represent average of 8 specimens.

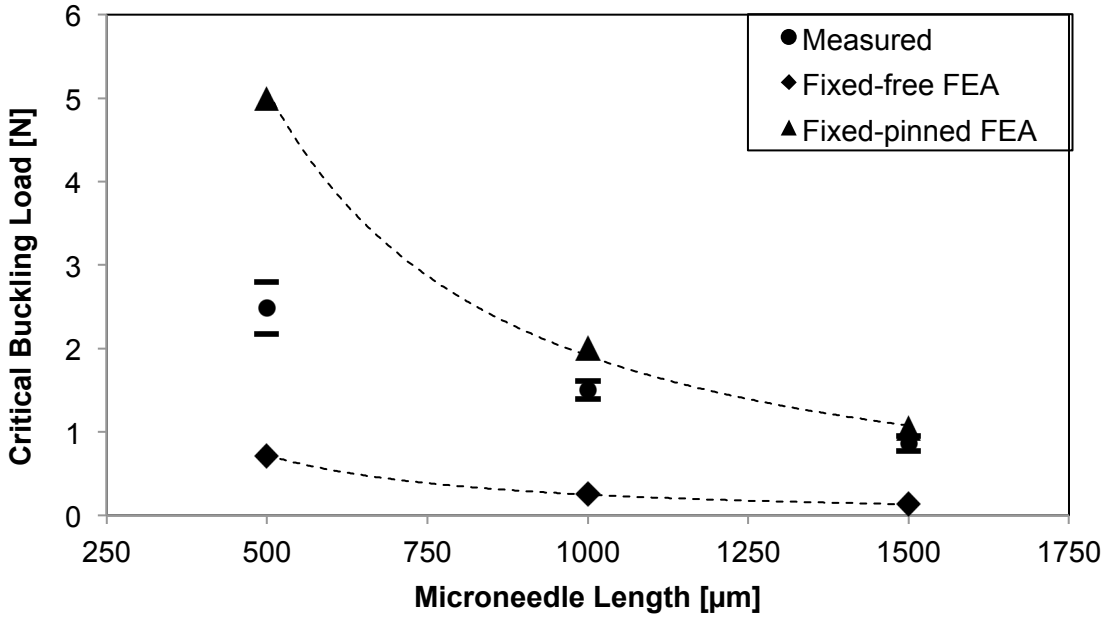

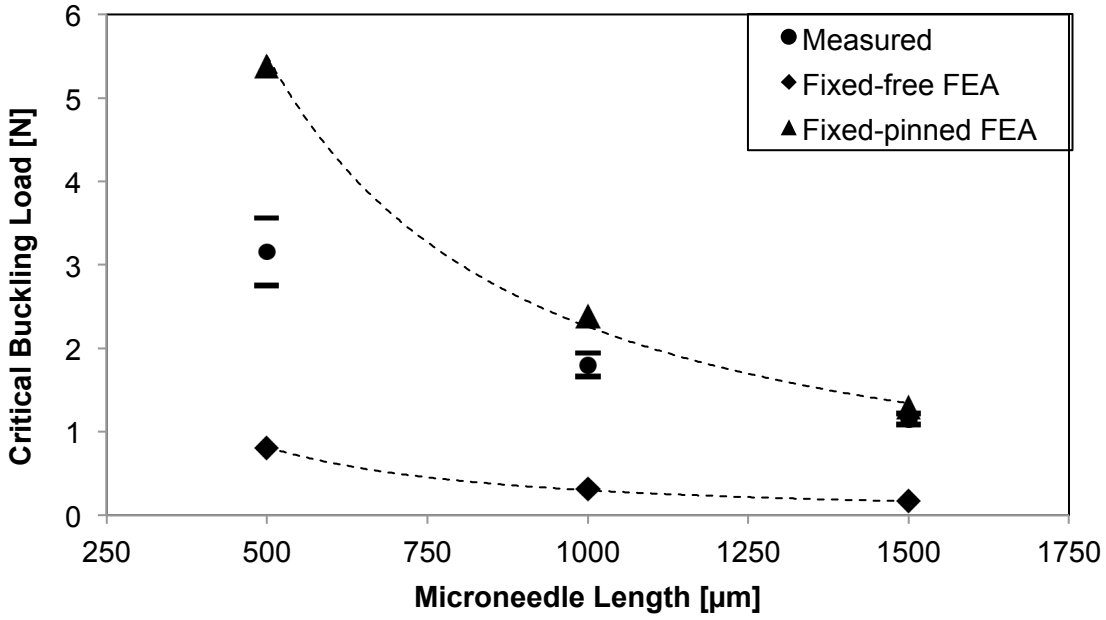

Figure F-2. Measured and FEA-predicted critical buckling loads for solid Ti MNs with varying μm width, 50 μm thickness, and 500 - 1500 μm lengths: a) 150 μm width; b) 200 μm width. Experimental data points represent average of 8 specimens.

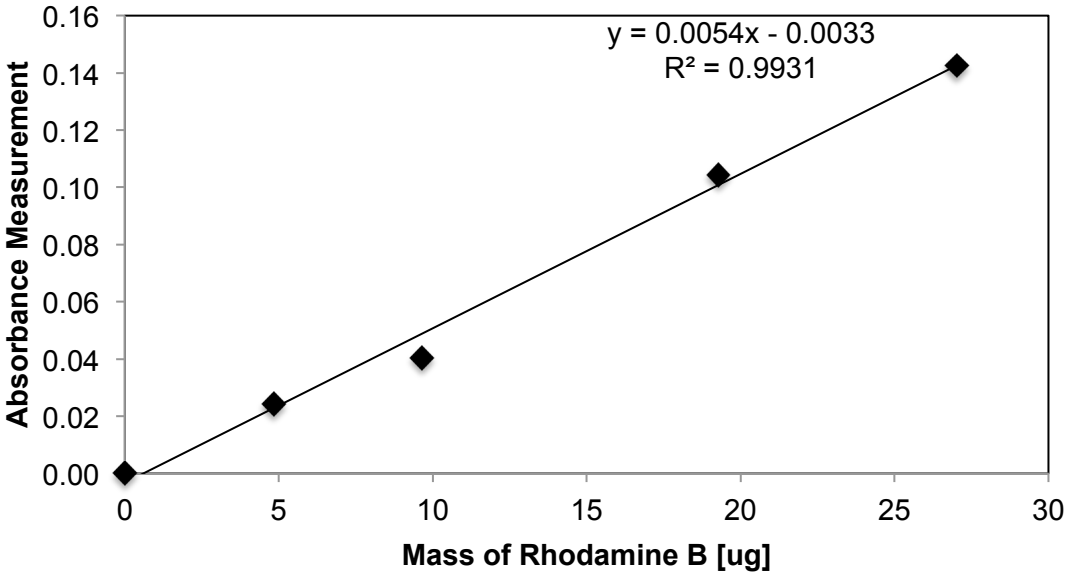

Figure F-3. Calibration curve of measured Rhodamine B intensity using the spectrophotometer.